GX 339−4: Spectral investigation of a black hole binary

GX 339−4: Eine spektrale Untersuchung des Doppelsternsystems mit schwarzem Loch

Bachelorarbeit aus der Physik

Vorgelegt von

Nico Wunderling

aus Fürth

der Naturwissenschaftlichen Fakultät
der Friedrich Alexander-Universität
Erlangen-Nürnberg

zur

Erlangung des Bachelor of Science B. Sc.

Betreuer: Prof. Dr. Jörn Wilms (FAU: Dr. Karl Remeis-Sternwarte, Bamberg)

FRIEDRICH-ALEXANDER UNIVERSITÄT ERLANGEN-NÜRNBERG
NATURWISSENSCHAFTLICHE FAKULTÄT

ERLANGEN CENTRE FOR ASTROPARTICLE PHYSICS

Ich versichere, dass ich die Arbeit selbstständig verfasst und keine anderen als die angegebenen Quellen und Hilfsmittel benutzt sowie Zitate kenntlich gemacht habe.

[Ort], den [Datum] [Unterschrift]

Nico Wunderling
Dr. Karl Remeis-Sternwarte & ECAP
Sternwartstraße 7
96049 Bamberg
Nico.nw.Wunderling@fau.de

Zusammenfassung

Das Thema dieser Bachelorarbeit ist die spektrale Untersuchung eines Röntgendoppelsternsystems mit einem schwarzen Loch. Dabei handelt es sich um ein System bestehend aus einem schwarzen Loch und einem normalen Stern, die sich um ihren gemeinsamen Schwerpunkt herum bewegen. In unserem Fall hat der normale Stern seinen sogenannten Roche-Radius, erreicht und verliert nun Materie an das schwarze Loch. Durch die dabei in Gang gesetzten Prozesse entsteht Röntgenstrahlung, die wir mit entsprechenden Röntgensatelliten nachweisen und quantifizieren können. Ein Vertreter dieser Klasse ist das Objekt GX 339−4. Wir untersuchen GX 339−4 in dieser Arbeit anhand von Messreihen mit dem Satellit RXTE, die während insgesamt acht Monaten aufgenommen wurden. In dieser Zeit durchlief unsere Röntgenquelle einen Helligkeitsausbruch und eine Phase relativer Ruhe.

Solche Doppelsternsysteme mit schwarzem Loch zeigen über die Zeit hinweg verschiedene Phasen unterschiedlichen Verhaltens, sogenannte „Zustände“. Typischerweise gibt es einen weichen und einen harten Zustand. Diese Zustände besitzen unterschiedliche Eigenschaften bezüglich ihrer emittierten Röntgenstrahlung. So ist der Anteil an hochenergetischer Röntgenstrahlung im Vergleich zur gesamten emittierten Röntgenstrahlung im harten Zustand höher als im weichen. Die Zustände an sich weisen nun vergleichbare, typische Konfigurationen von Strahlungsquellen auf, z.B. einen Jet im harten Zustand oder eine starke Akkretionsscheibe im weichen Zustand. Daher beschäftigt sich ein Großteil dieser Arbeit damit, diese Zustände einzuteilen und zu untersuchen. Wir wenden dabei Methoden wie „hardness intensity“ Diagramme und „disk fraction luminosity“ Diagramme an, genauso wie eine Zustandsunterscheidung anhand der An- bzw. Abwesenheit einer Akkretionsscheibe in unseren spektralen Modellen. Das Ergebnis dieser Untersuchungen ist, dass es uns anhand solcher Methoden vergleichsweise leicht fällt die verschiedenen Zustände zu unterscheiden und zu charakterisieren.

Des Weiteren benutzen wir zwei empirische Fitmodelle, nämlich ein “powerlaw” und ein “broken powerlaw”, da verschiedene physikalisch motivierte Modelle die Beobachtungsdaten gleich gut erklären, sodass wir nicht entscheiden können welches dieser Modelle die physikalische Realität am besten widerspiegelt. Eines der benutzten empirischen Modelle ist ein einfaches Potenzgesetz, das andere besitzt einen Bruch bei einer bestimmten Energie, typischerweise zwischen 7 und 15 keV. Wir vergleichen die beiden Modelle anhand der Güte der Fits, die mit ihnen möglich sind. Wir stellen fest, dass es manchmal gerechtfertigt ist mehrere dieser Potenzgesetzmodelle miteinander zu verschmelzen je nach dem, wo sie am besten funktionieren. Ein solches Vorgehen ist dann erlaubt, wenn die jeweils benutzten Parameter bei den beiden Modellen nahezu identische Werte aufweisen. Insgesamt stellt sich heraus, dass das Potenzgesetz mit Bruch die Daten etwas besser beschreiben kann als das einfache Potenzgesetz. Ein solches Ergebnis ist aufgrund der zugrunde liegenden physikalischen Prozesse wie der Comptonisierung und der Reflektion zu erwarten.

Abstract

In this bachelor thesis we investigate spectral properties of a black hole binary. A black hole binary is a system, in which a normal star and a black hole orbit their common barycenter. In our case the normal star has approached its Roche-radius and looses mass to the black hole. Because of processes that came up with this circumstance, X-ray radiation arises, which we can prove and quantify using X-ray satellites. A representative of this type is GX 339−4. We investigate GX 339−4 in this work using a measurement series with the RXTE satellite that were recorded during eight months. In this period our X-ray source had one brightness outburst and a phase of relative quiescence.

Such black hole binary systems show phases of different behavior, so called “states”. Typically, there is a hard and a soft state that have different properties in terms of their X-ray radiation. For example, the amount of high energetic X-ray radiation compared to the total X-ray radiation is higher in the hard state than in the soft. The states are characterized by comparable configurations of radiation sources, e.g., by a jet in the hard state or a strong accretion disk in the soft state. A big part of this thesis therefore pursues the goal to disentangle these states. We apply methods like “hardness intensity” diagrams or “disk fraction luminosity” diagrams as well as state distictions using the presence or absence of an accretion disk in our spectral models. The result of this investigation is that it is comparatively easy to distinguish and to characterize the different states with these methods.

Furthermore we use empirical fit models, namely powerlaw and broken powerlaw models, as various physical motivated models explain the observed data equally well, so that we cannot decide which of these models reflects the physical reality best. One of these powerlaw models is a simple powerlaw whereas the other one is a broken powerlaw with a typical break energy between 7 and 15 keV. We compare our two models by means of their fit goodness. We assess that it is justified to merge several of these powerlaw models depending on where they work best. Such a procedure is permitted when the fitted parameters yield nearly the same values, no matter if the powerlaw or the broken powerlaw model is used. Altogether it comes out that the broken powerlaw fits the data a little bit better than the simple powerlaw, as expected given the underlying physical processes such as Componization and reflection.

Contents

Chapter 1

Introduction

You have to start with the truth. The truth is the only way that we can get anywhere. Because any decision-making that is based upon lies or ignorance can't lead to a good conclusion.

Julian Assange

As the quotation dictates we have to start with the "truth". The truth is we don't know very much about black holes and their physical processes from direct observations, so nearly all the information about appearance and properties are results from calculations and models. But what does that mean for our "truth"? It means that the real visual appearance could be quite different to the appearance that models give us and therefore the models sometimes simulate a "truth" that actually is not present. So it is our task in this work to cut our way through the jungle of models and winkle out a grain of "truth".
That's why we start with the foundations of physics related to black holes and black hole binaries on the basis of models in Chapter 2. First of all fundamental comprehension for the type of objects should be gained, whereupon a Section about the specific object GX 339−4 is attached. Subsequently we want to concentrate on more models, in which we can learn something about the geometry of black hole binaries and, furthermore, in this Section we want to focus on radiation processes. We consciously do not want to describe these radiation processes in their full mathematical beauty, they can be looked up in corresponding literature. We will give references to that literature in the according passage. A very important point in our model Section are the hardness intensity diagrams which will be explained in that part, too.
Afterwards in Chapter 3 we give a description of the satellite and its recording possibilities so that we first know what RXTE acchieve.
Upon this theoretical background knowledge and physical explanations we continue this thesis with our used spectral models, a powerlaw model and a broken powerlaw model, in Chapter 4. We include a detailed explanation of these models in this Section. We show spectra of GX 339−4 and conclude that our source is a typical object of its class. The following Sections contain a part about state distinctions based on the accretion disk and hardness intensity diagrams of GX 339−4. Finally we draw a conclusion and an outlook in Chapter 5.

Chapter 2

Physical fundamentals of black hole binaries

Einstein was wrong when he said, "God does not play dice". Consideration of black holes suggests, not only that God does play dice, but that he sometimes confuses us by throwing them where they can't be seen. *Stephen Hawking*

Black holes are among the most mystified objects in our cosmos. For example, you can watch some "terrifying" TV-reportages about silent black holes flying through our galaxy, getting awake in a flyby near our solar system and gorging everything coming towards them. Well, such "all-eating" –black holes are rather unlikely to exist, but anyway, black holes are some of the most interesting and fascinating astronomical objects. Hence there is spent "a certain extent [...](of) the tax-payers' money" on their investigation (citation from Wilms, 1998, page 10). Long before the theoretical foundation of a black hole (general relativity and calculations by Karl Schwarzschild, 1916) John Mitchell showed at the end of the 18th century that even light cannot escape from a sufficient massive compact object and created the theoretical basis for black holes (Wilms, priv. comm.). So black holes have a long history. But this is not the only reason why black holes are interesting objects for scientific investigations – they are also extreme objects and so they allow us to test our understanding of physics under extreme conditions. In general there are two main groups of observed black holes, the supermassive black holes in the center of galaxies and the stellar black holes. One of the latter black holes is subject of this bachelor thesis. A system consisting of such a stellar black hole and a companion (usually a "normal" star) is called a Black Hole Binary (BHB). It emits characteristic radiation mainly in the X-ray range. In the following Section we want to describe stellar BHBs.

2.1. Black Hole Binaries

Before we can speak of a Black Hole Binary we have to know what the companion of the visible star is, i.e., whether it is a black hole, a neutron star, or something else. As that cannot be easily determined we have to go a step back. At first these binary objects have a high X-ray flux and a (usually) visible companion star. We can distinguish two different kinds (adopted from Grinberg, 2013):

- High mass X-ray binaries (HMXBs): The companion star has a high mass, i.e., is an O-, A-, or a B-star. Accretion is fed by stellar winds that are relatively high in this type of stars
- Low mass X-ray binaries (LMXBs): The companion star is a low mass star, i.e., a G-, K-, M-,

or a L-star. Accretion occurs due to the companion star filling its Roche lobe and loosing mass that crosses the Lagrange point L_1 (Karttunen et al., 2006)

One very useful possibility to distiguish a neutron star from a black hole is the mass of the compact companion. If it is above 3 $M_\odot$, we can conclude that the invisible object is a black hole as the Oppenheimer-Volkoff (see Oppenheimer et al., 1939) mass limit restricts the maximal stable mass a neutron star can have can have to about 3 $M_\odot$. To this date we know about 20 black hole binaries as well as some additional candidates. In Remillard et al. (2006) the known black holes binaries oder black hole binary candidates in the Milky Way are listed, see also Fig. 2.1. Predictions estimate over 10^8 stellar black holes in our galaxy[1] (Shapiro et al., 1983) with about 35,000 in our direct neighbourhood (250 pc, Fender et al., 2013).

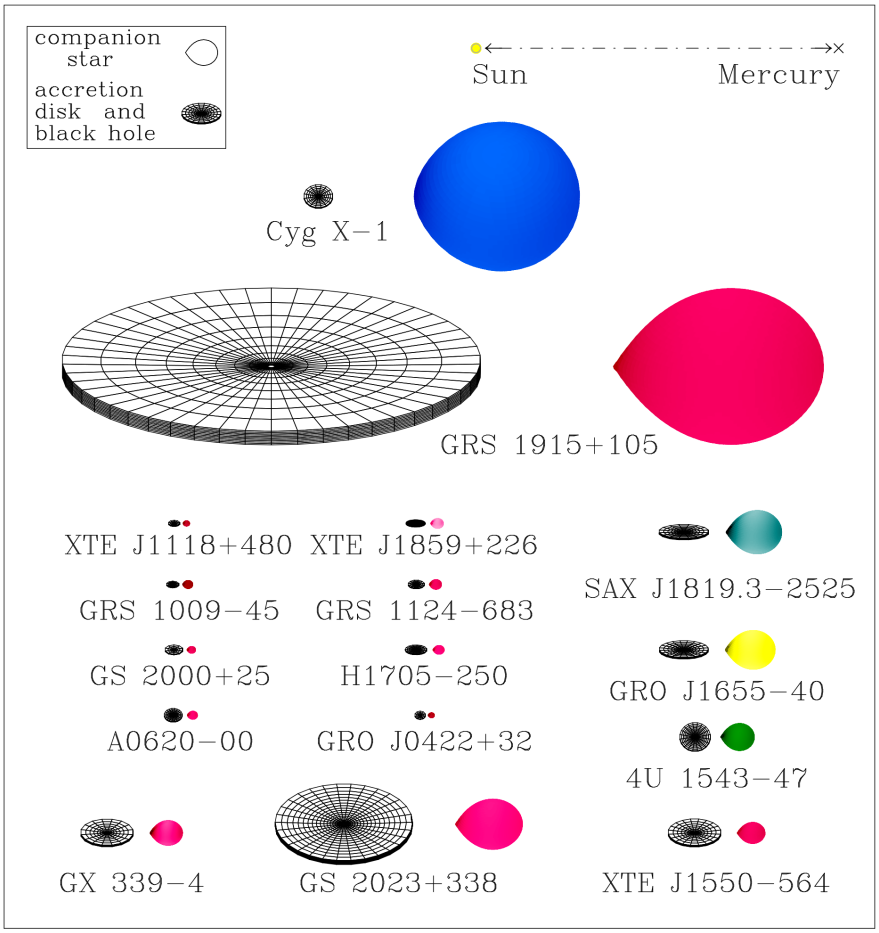

Figure 2.1.: Some known black hole binaries in the Milky Way. The distance from Mercury to the Sun (0.39 AU) is shown on the top right hand side for orientation. The inclination is indicated by the tilt of the accretion disk and the color of the companion star indicates its temperature. Blue is hotter, red is colder. GX 339−4, examined in this thesis, is in the bottom left corner. Figure from Remillard et al. (2006)

[1] Probably that number is estimated too high (Wilms, priv. comm.)

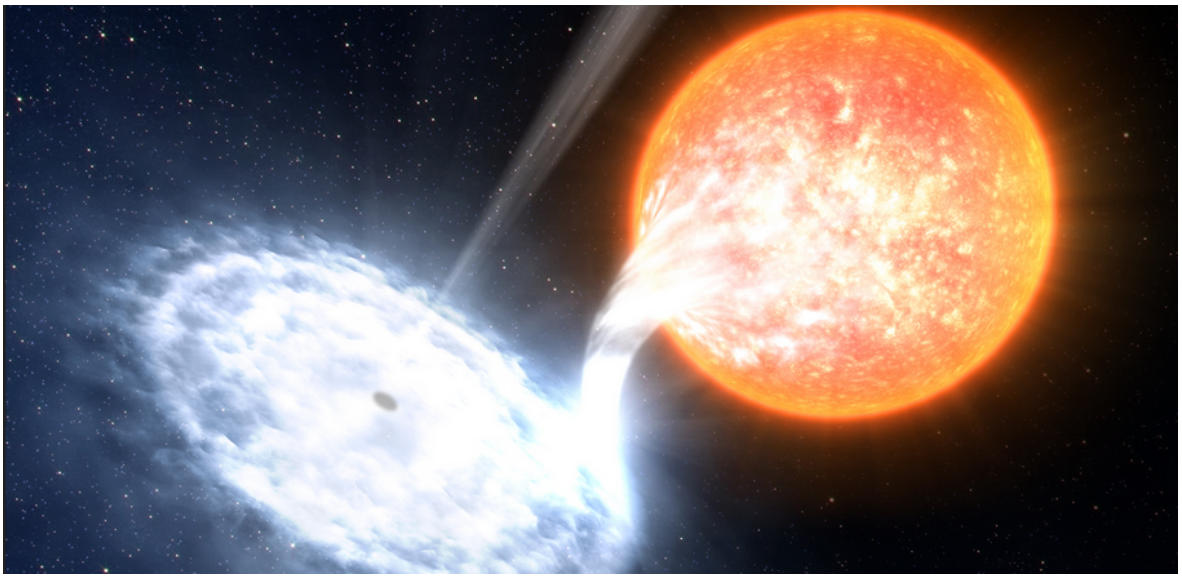

Figure 2.2.: Artistic impression of GX 339−4. On the left side we see the black hole with its external accretion disk and a jet, i.e., it is in a hard state (definition of states in Sect. 2.3.1). On the right hand side the companion star is orbiting around the black hole. Figure from G. Ruprecht (ESO Garching).

2.2. GX 339−4

In this Section we describe the black hole binary GX 339−4 and its companion star in more detail. An artistic impression of GX 339−4 is shown in Fig. 2.2.

Distance

GX 339−4 is located in the constellation Ara near the Galactic center. The distance is not easy to determine and is highly disputed. Hynes et al. (2004) believe GX 339−4 has a distance of about 6 kpc, while Zdziarski et al. (2004) estimate that the distance is greater than 7 kpc. Both of them cannot exclude each others results. Furthermore the companion star cannot be seen in the faintest observations. This could be explained by a very great distance, for example GX 339−4 being located on the other side of the Milky Way, that means a distance of more than 15 kpc (Hynes et al., 2004). So the determination of the distance remains uncertain.

Mass

The companion star is a low mass star (spectral type G, K, M, or L). Its optical magnitude and therewith its spectral type could not be determined yet. We see differences in the magnitudes of the binary system (15 mag in the hard state to 19.5 mag in the faintest states, see Buxton et al., 2012), but we have to assign them to the jet and the accretion disk as well as to the optical companion (Grinberg, priv. comm.). So the determination of the companions' spectral type remains uncertain. The estimated mass of the companion is 0.3 $M_\odot$ (with a maximum possible mass of 1.1 $M_\odot$, see Muñoz-Darias et al., 2008). This gives rise to a compact mass slightly above 7 $M_\odot$ (Muñoz-Darias et al., 2008), so the compact object must be a black hole. An exact measurement consistent with that latter value is given by Chen (2011) with $M_{BH} = 7.5 \pm 0.8\ M_\odot$. We can therefore conclude GX 339−4 is a LMXB. The orbital period of the two objects is 1.7557 ± 0.0004 days (Muñoz-Darias et al., 2008).

Size

The relative size and the separation of the secondary star and the black are stitched in Fig. 2.1. We can assess from the figure that GX 339−4 and its companion is a tight bound system with a separation of only a few solar radii. The size of the black hole with an estimated mass of 7.5 $M_\odot$ is about 22.5 km. The size of the companion star cannot be determined clearly but it is assumed that the star fills its Roche lobe.

Spin

The spin of a black hole can be estimated by determining the iron line profile, which become more broadened and skewed with greater values of the black hole spin (Fabian et al., 1989, see also Fig. 2.5). The variable a, known as the spinning paramater of a BH, lies between 0 and 0.98. The latter value is assigned to a maximally rotating BH. With that procedure Yamada et al. (2009) get $a < 0.4$, a not very fast rotating black hole. Due to problems of fitting the iron line correctly there are some doubts about these results. There were measurements of the BH spin that resulted in $a \approx 0.9$ (Miller et al., 2008), a fast rotating BH. So the spin measurement of GX 339−4 remains uncertain. For a more precise discussion about the spin of black holes in general see Dauser (2014).

Inclination

The exact inclination is not yet known but inclination angles between 0 – 20° and 50 – 90° can be ruled out because of the radiation coming towards the earth, so edge-on and face-on geometries are not possible. That means the inclination has to be in a medium range between 20° (Petrucci et al., 2014) to about 45 – 50° (Maitra et al., 2009).

HI

The amount of neutral HI (measured using the 21 cm line) in the line of sight is about $5 \cdot 10^{21}$ cm^{-2} (see Kalberla et al. (2005) or Miller et al. (2004)).

2.3. Spectra and their explanation

2.3.1. Geometry

Basically for all BHBs there are two different spectral states, a so called *hard* (previously called *low*) state and a *soft* (previously called *high*) state. This behavior was first discovered by Tananbaum et al. (1972) in Cyg X−1. The two states are generally quite different looking at all wavelength. Beginning with the hard state, in many BHBs we observe that the amount of radio emission is positively correlated with the amount of X-ray emission (Gallo, 2010). The source of the radio emission is a jet. This radio – X-ray correlation is also proved for GX 339−4 (Gallo, 2010). One reason for this could be the Compton up-scattering so that the radiation is up-scattered to the X-rays by electrons out of the jet base or a corona. Also, synchrotron radiation of the jet could contribute to the X-ray radiation (Grinberg, 2013 and references therein). The X-ray spectral shape, looking like a broken powerlaw, is due to that Comptonization from the jet or the hot corona, see Fig. 2.3 left side. That is one of the geometries favored today but one cannot exclude other geometries. Some of them are shown in Fig. 2.3 right side. Furthermore, as already mentioned, the disk is not visible in some observations in the hard state in the energy range used in this work.

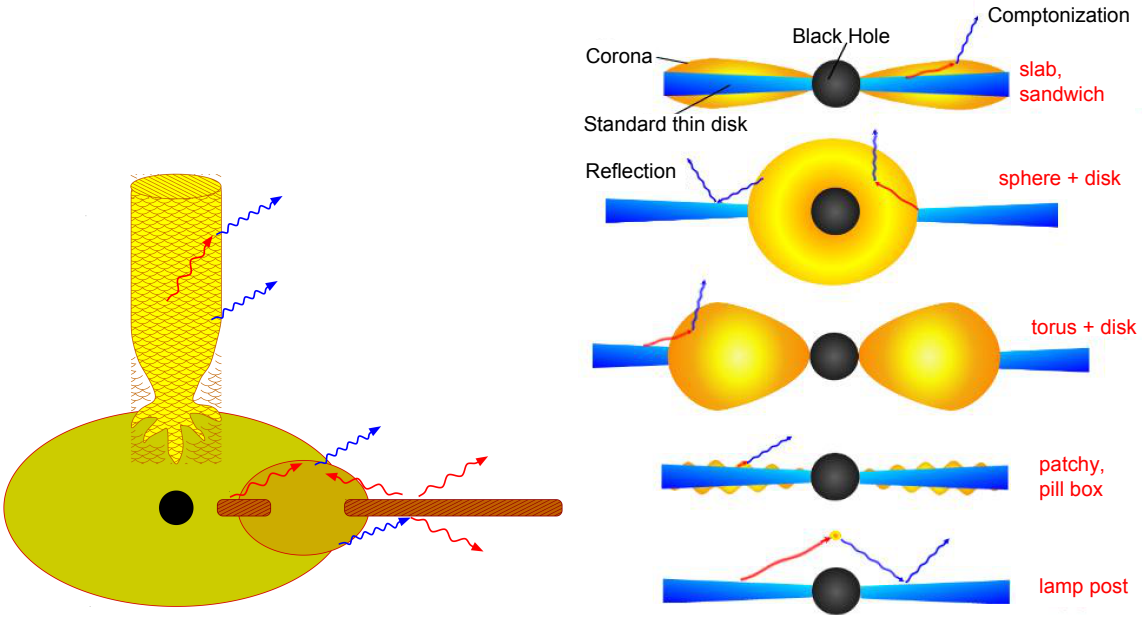

Figure 2.3.: Left: Two possible geometries of a black hole binary in the hard state. At first, in brown, the truncated disk with two possible geometries of the corona. The torodial geometry in light brown or a spherical geometry in an odd mixture of yellow and green. A possible jet is shown in yellow above the black hole. In red and blue there are shown the reflected and Compton up-scattered photons (red for less energetic photons, blue for higher energetic photons). Also photons from the corona reflected by the standard thin disk are possible. Figure from Nowak et al., 2011. **Right**: Some other possible geometries like a lamp-post geometry (used to explain the relativistic broadening of the iron line, see Dauser, 2014), a slab like geometry (used by Malzac et al., 2000) or a sphere plus disk (used by Dove et al., 1997) model and some more. Figure from Müller, 2007.

In contrast to the hard state, the radio emission in the soft state is strongly suppressed (Grinberg, 2013 and references therein).
That means in the soft state we don't have a jet or at least a very weak one. In the X-ray regime the both states can be described with the same model components, namely a powerlaw or a broken powerlaw model both with a blackbody disk. The parameters of these models vary in relative strength between the states of the source. A typical distinction possibility is the slope of the fitted powerlaw, called *photon index* Γ. In the rest of this thesis we want to use the following state distinctions:

1. hard state: $\Gamma < 1.8$

2. soft state: $\Gamma > 2.0 - 2.5$

The states can also be defined by a so called hardness intensity diagram (HID, see, e.g., Dunn et al. (2008)). The hardness is defined by the fraction of the count rates or fluxes of one energy band (usually the higher energy band) through another (usually the lower energy band). The intensity is defined by the total counts in an energy band per exposure time or, as it is here, by the X-ray luminosity in a wide energy band. Some of such HIDs can be found in Figs. 4.9. A figure of a model HID is shown in Fig. 2.4 from Dunn et al. (2008). A q-shaped structure can be seen clearly. Some physical meanings of states are shown around the middle box. Further details will be shown and explained in Sect. 4.

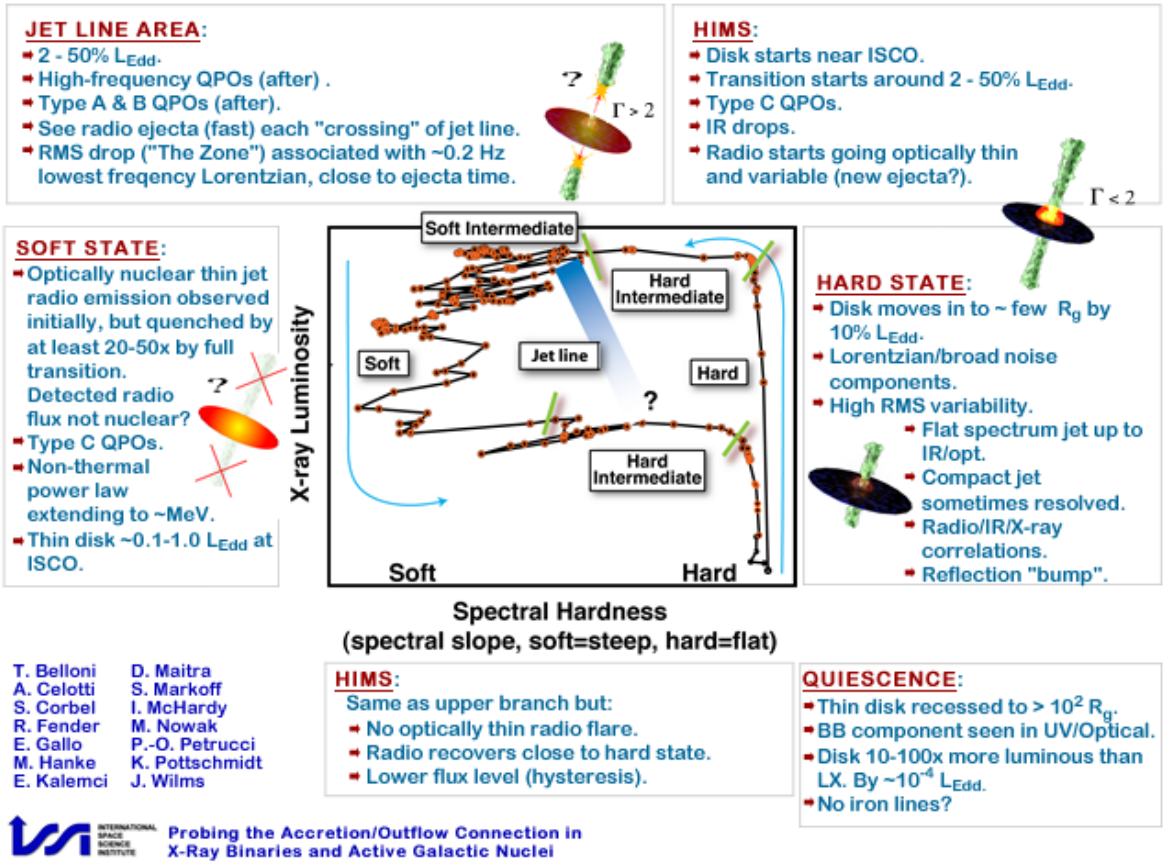

Figure 2.4.: A q-shaped track of a black hole binary on a HID. Figure from `http://www.sternwarte.uni-erlangen.de/proaccretion/states/index.html`, date: 07.07.2014

2.3.2. Models

Before we investigate the observed BHB GX 339−4, we want to elucidate the reason why our chosen fitting model is not based on a physical model but more on an empirical description. Therefore in this Section we will talk about a few physical processes that are typically thought to produce the energy spectrum of a BHB. Figure 2.6 (left panel) shows a typical X-ray spectrum with an example model, here with thermal electrons, i.e., electrons in a Maxwell-Boltzmann-distribution. The model of the data is shown in orange and contains several components.

1. **Accretion disk(s) and its black body radiation** (dominant between 0.1 and 5 keV):
   The accretion disk is visible in the soft X-rays and emits blackbody radiation. Sometimes it cannot be seen in the hardest spectral observations above 3 keV. In such cases the disk is weak and its temperature low (Grinberg, priv. comm.). Thus we fitted every observation with and without a disk.

2. **Comptonization and reflection hump** (dominant between 3 and 300 keV):
   So called seed photons reach the hot corona probably arising from the cold material (for geometry of corona and accretion disk see also Sect. 2.3.1) from the accretion disk[2]. There, the

[2]typical temperatures of accretion disks scale about 1 keV $\approx 10^7$ K (Dove et al., 1997), coronal temperatures are about 150 keV $\approx 2 \cdot 10^9$ K (Nowak et al., 2011), that means the corona is a factor 200 hotter. So accretion disks with a temperature of 10 million Kelvin are really cold for X-ray astronomers.

seed photons are Compton up-scattered by ultrarelativistic thermal distributed electrons, so an electron hits a photon and scatters it to higher energies[3] (Müller, 2007). With these processes not only galactic black holes can be explained but also Active Galactic Nuclei (e.g., NGC 4151, Zdziarski et al., 1996). The reflection hump arises from photons out of the hot corona (see Fig. 2.3) or a jet. These photons hit the accretion disk and will then be reflected (Nowak et al., 2011). In the case of an inner and an outer disk, the outer disk contributes the major part of the reflection (Nowak et al., 2011). The total shape of Componization plus reflection gives a powerlaw or broken powerlaw like appearance.

3. **Relativistic broadened iron line** (important between 6 and 7 keV):
   Strictly speaking we talk about the Kα Fe-line at 6.4 keV (Müller, 2007). Based on that line, we already mentioned that the spin of a black hole can be measured (Dauser, 2014). In our spectral analysis we assume that the iron line is Gaussian, but indeed it is not. Due to hot material in the corona and material in the accretion disk, relativistic effects (e.g., Beaming or gravitational redshift; see Dauser (2014) or Müller (2007)) are important to describe the proper shape of the Fe-line, see Fig. 2.5 in an extreme example. Because of the modest spectral resolution of RXTE (see Chapt. 3) the Gaussian shape of the Fe-line is despite sufficient for good fits.

4. **Absorption** (especially important near absorption edges):
   Absorption of photons with a certain energy can occur due to absorbing atoms, especially near their absorption edges, see Dauser (2014, page 47). Such atoms can be located either in gas clouds in the interstellar medium in the line of sight (interstellar absorption) or directly around the black hole binary (intrinsic absorption). The interstellar absorption can be modelled with tbnew (for explanation see Sect. 4.1), but the absorption due to GX339−4 (e.g., due to the accretion disk) itself is not modelled in this thesis. Absorption is not a modelled part in Fig. 2.6.

For further details in a more descriptive way see Müller (2007, in german), a short concise overview about radiation processes can be found in Graefe (2014). More details about radiation processes are in Rybicki et al. (1979) and, if you are interested in accretion physics, see Frank et al. (2002). The iron line and reflection models are described exhaustively in Dauser (2014). The model shown in Fig. 2.6 left panel is not the only one that could explain the data points, but there are at least two more physical motivated models (an exact description of all three models can be found in Nowak et al., 2011), see Fig. 2.6 middle and right panel. That means we cannot determine the exact physical model because each of the three models can be fitted to the data points with a comparable statistical goodness and so we don't have any distinction or preference of any of these models. Out of this reason we decided to take purely empirical models. They are described in detail in Sect. 4.1.

[3] reverse to the "normal" Compton effect

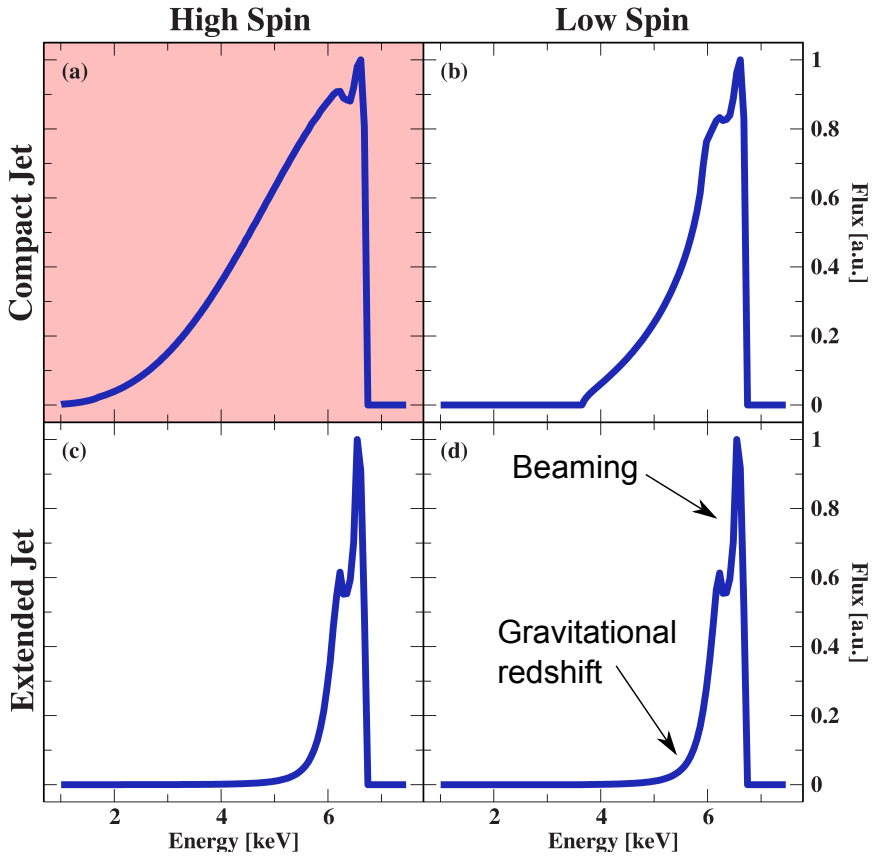

Figure 2.5.: Relativistic not symmetrically broadened iron line shape in the cases of compact and non compact jet as well as for low (a = 0) and high spin (a = 0.99) of the black hole. For more information see Dauser et al. (2013). Figure adapted from Dauser et al. (2013).

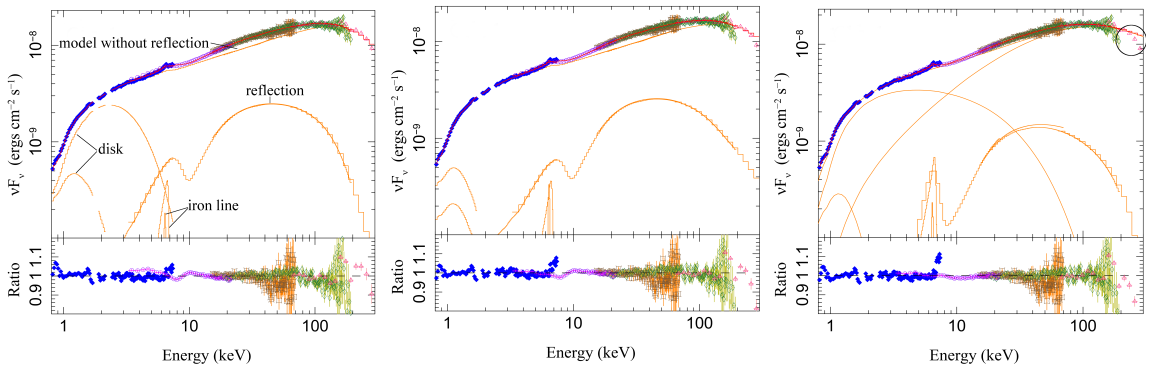

Figure 2.6.: Left: X-ray spectrum of a hard state of Cyg X−1. Compare data points and model (thermal coronal electrons) which explain the data. **Middle**: X-ray spectrum with non thermal coronal electrons, i.e., electrons out of a non thermal velocity distribution (power law distribution). **Right**: X-ray spectrum with a jet model. The Klein-Nishina cross section (black circle) was not yet included in the jet model, so in the very high energy bands there is a little deviation from theory and measured values (Wilms & Grinberg priv. comm. and Grinberg, 2010). Figures adapted from Nowak et al. (2011).

Chapter 3

Instrumentation: Rossi X-ray Timing Experiment

How is it possible that results bearing on fundamental problems of elementary particle physics could be achieved by experiments of an almost childish simplicity, costing only a few thousand dollars and requiring only the help of one or two graduate students? *Bruno Rossi*

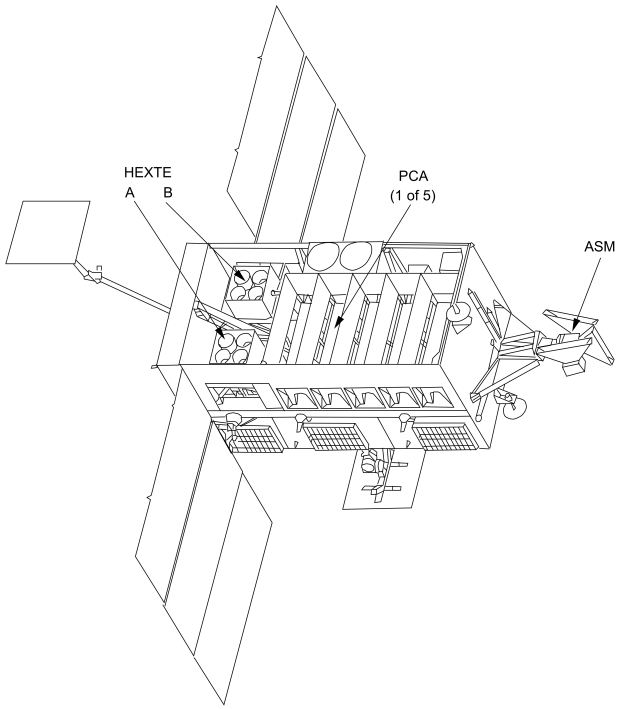

Figure 3.1.: Scheme of RXTE. The All Sky Monitor (ASM) is located on the right hand side with an uncovered view to almost the whole sky. The Proportional Counter Array (PCA) with its five rectangular arranged Proportional Counter Units (PCUs) is in the middle. The two square boxes on the left side constitute the High Energy X-ray Timing Experiment (HEXTE). Each of the two HEXTE clusters contain 4 detectors. The two star trackers that are used to determine the current position of the satellite are above the PCA. Two antennas for the data exchange with the Earth are on the bottom and left side. The solar panels for power supply are on the top and the bottom of the satellite. Figure from Rothschild et al., 1998.

The Rossi X-ray Timing Experiment (RXTE; Bradt et al., 1993; see Kreykenbohm, 2004 or Wilms, 1998 for a summarizing overview) is a X-ray satellite that was built to investigate spectral and timing phenomena of compact stellar and galactic objects like pulsars or black hole binaries. It was launched from Cape Canaveral on 30 December 1995 and decommissioned on 5 January 2012. During that time the satellite took data from various sources. The mass of RXTE was 3038 kg with an initial flight altitude of 580 km and an inclination of 23°. One orbital period lasted about 90 min. Because of some altitude loss over the years, RXTE is expected to fall back into Earth's atmosphere some time between 2015 and 2023. RXTE had three onboard devices, the Proportional Counter Array (PCA; Jahoda et al., 2006; Shaposhnikov et al., 2012), the High-Energy X-ray Timing Experiment (HEXTE; Rothschild et al., 1998) and the All Sky Monitor (ASM; Levine et al., 1996). The All Sky Monitor was a device that is scanning over 70% of the sky during one orbit. That is worthwhile because the X-ray sky is highly variable, sometimes on timescale of minutes. If the ASM discovers something peculiar, RXTE can quickly look at that source with its fast slewing velocity of 6°/minute. Figure 3.1 shows the RXTE–satellite.
A rather challenging problem for all satellites are the so called "Van Allen belts", named after their discoverer James van Allen (van Allen, 1958; van Allen et al., 1959). The Van Allen belts are a torus of charged particles around the Earth. The particles are caught by the Earth's magnetic field and held in there. The ionized particles originate from the radiation belt itself (Reeves et al., 2013). Strong electric fields ionize the atoms, accelerate the electrons and the atoms and distribute them in the Van Allen belts. A first belt that mainly consists of high-energetic protons is located 700 – 6,000 km above the surface of the Earth. A second belt that mainly consists of relativistic electrons lies further outside, at 15,000 – 25,000 km. That alone would not be a problem for RXTE due to its flight altitude of 580 km. But because of the non-circularity of the magnetic dipole field and the Earth not being spherical, there is a region of weak magnetic fields, the so called South Atlantic Anomaly (SAA, for more information see Fürst et al., 2009). In this region, shown in Figure 3.2, the Van Allen belt comes down to about 200 km above the Earth. Here the radiation of SAA protons overlies the radiation of observed X-ray sources in the sky so that a serious scientific analysis cannot be done while RXTE is passing through the SAA. That is why RXTE was shut down or the high voltage of the Proportional Counter Units (PCUs), described in the next Section, are lowered while going through the SAA.
For further information on the RXTE satellite see the official website of RXTE[1] and the technical appendix of RXTE[2]. Scientific data used in this thesis are from PCA and HEXTE. So we concentrate on these two devices in the following Sections.

3.1. Proportional Counter Array (PCA)

The Proportional Counter Array (Jahoda et al., 2006) was built at the Goddard Space Flight Center (GSFC) in Greenbelt, Maryland. It consists of five Proportional Counter Units (PCUs), one of those shown in Fig. 3.3. Each PCU has a collimator with an angular resolution of 1°. If the angular distance of two X-ray sources is smaller than 1° they cannot be resolved properly, although there are some techniques like off-center observations (i.e., one source is outside of the field of view) that may still allow to disentangle such sources. Below that collimator there are two Mylar windows, one above and one below a propane veto layer. They are followed by the three main Xenon layers, where an incoming photon is detected. The calibration source ^{241}Am (α–radiator with a characteristic energy of 59.6 keV) and the alpha detector are mounted below the last Xenon layer.

[1] `http://heasarc.gsfc.nasa.gov/docs/xte/XTE.html`
[2] `http://heasarc.gsfc.nasa.gov/docs/xte/appendix_f.html`

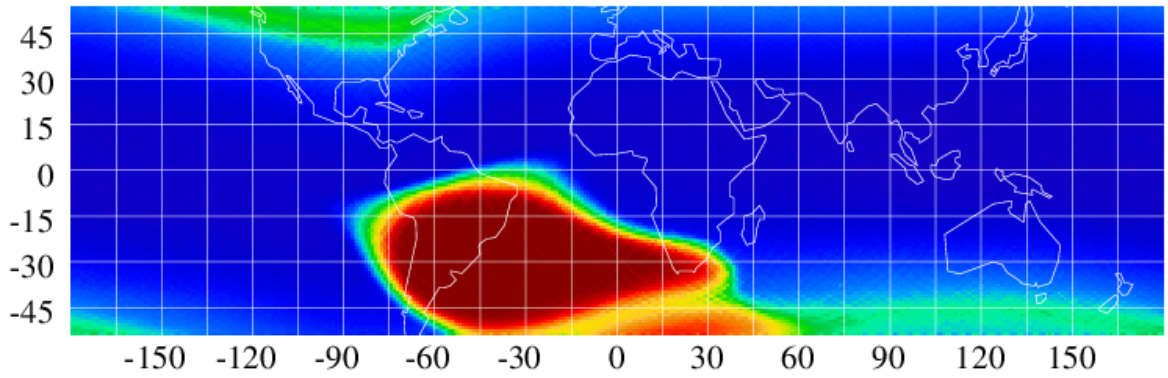

Figure 3.2.: The South Atlantic Anomaly (SAA) measured by ROSAT. An intesity maximum of radiation can be seen in the south-east of the Brazilian coast. Figure from Snowden (2002).

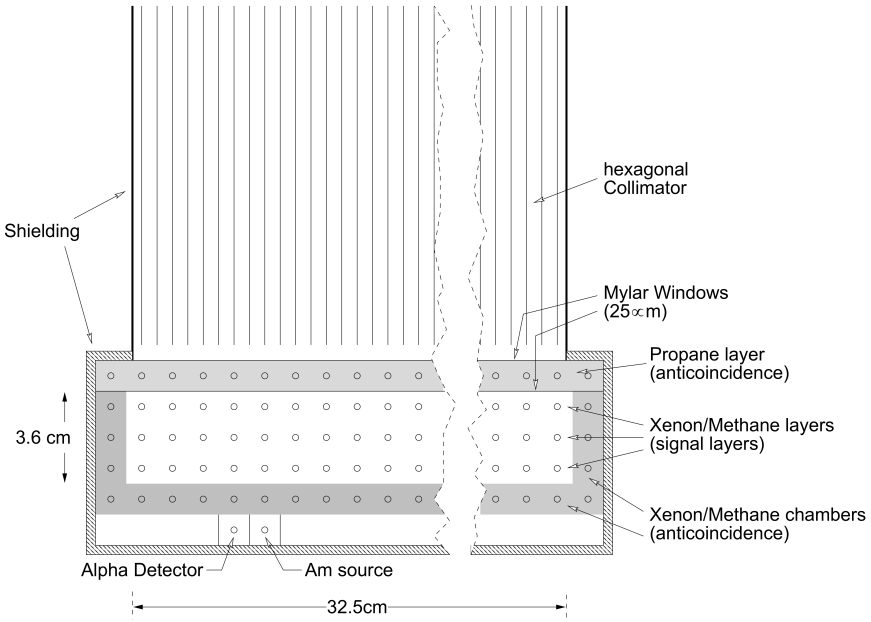

Figure 3.3.: One of five Proportional Counter Units, description see text. Figure from Wilms (1998).

3.1.1. Background radiation

The background radiation of PCA consists mainly of three components that have to be considered (Kreykenbohm, 2004), see also left side of Fig. 3.4:

1. diffuse X-ray background of unresolved AGN or other X-ray sources
2. local particle background of protons and electrons that react similarly to X-ray photons
3. induced radioactivity of the spacecraft by high-energetic particles like particles from the South Atlantic Anomaly, see Fig. 3.4, right side

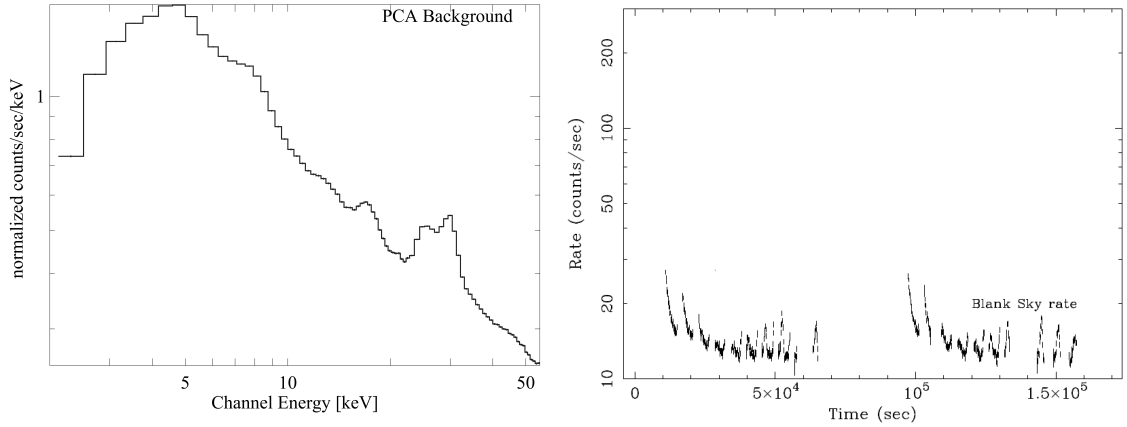

Figure 3.4.: Left: PCA background radiation. The emission lines between 4 and 5 keV are due to the Xenon L edges (4.78, 5.10 and 5.45 keV). The strong line at about 30 keV is caused by the Xenon K edge (34.6 keV). Some other peaks arise from induced radioactivity like the passage through the SAA. Figure adapted from Kreykenbohm (2004). **Right**: Two day observation of the blank-sky. Beside some orbital variations the typical 240 minutes decay of induced radioactivity from the passage through the SAA can be seen. Data is shown for all PCU 2 layers, the observation gaps are due to observations of other sources. Figure from Jahoda et al. (2006).

3.1.2. Energy resolution und limits

The RXTE-PCA has a source detection range from 0.3 counts s^{-1} PCU^{-1} in the 2 – 10 keV band to 20,000 counts s^{-1} PCU^{-1} (Jahoda et al., 2006). Above that limit the PCA has to be shut down to not sustain any damage. The energy resolution can be expressed (after Wilms, 1998) as:

$$\frac{\Delta E}{E} = 0.18 \cdot \left(\frac{E}{6\,\mathrm{keV}}\right)^{-1/2} \tag{3.1}$$

Here ΔE ist the Full Width at Half Maximum (FWHM) at the energy E. So the energy resolution is getting worse with greater E. At 6 keV the energy resolution is 18% ($\hat{=}$ 1 keV) which is a rather modest resolution. Narrow emission lines in spectra therefore cannot be resolved but the broad iron line that will be very important in our spectral analysis, can, although it is broadened up. The nominal geometric area of all five PCUs is about 8,000 cm^2. The effective area that is strongly depending on the energy (see Fig. 3.5) is not as large as the possible geometric area. The weak dips seen on Fig. 3.4, left, at 4.78 keV, 5.10 keV and 5.45 keV are the Xenon L edges, the big peak at 34.6 keV is the

Xenon K edge. According to Fig. 3.5 it is understandable that we only use the PCA data from 2.5 to 40 keV in our analysis with the following constraint. If the signal-to-noise ratio is smaller than five, the data is rebinned so that the ratio of counted photons to the poisson noise is at least five. That means the energy resolution is deteriorated. In general PCA data, although available between 2 and 100 keV, we only use them between 2.5 and 40 keV. For a cross-check between PCA and HEXTE, we also include the energy between 20 and 40 keV. We can determine the multiplicative constant (see Sect. 3.3) of the HEXTE cluster more precisely, if the overlapping energy bands between these two devices are bigger.

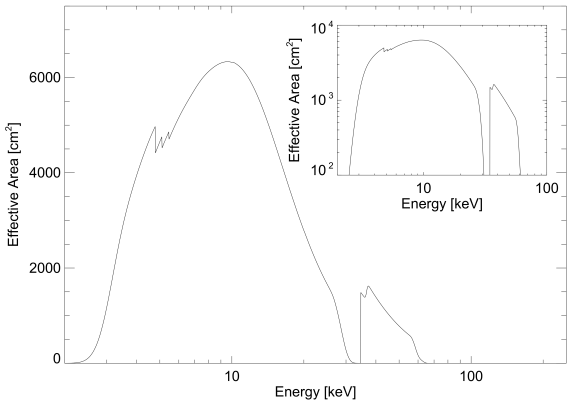

Figure 3.5.: Effective area of all five PCUs with logarithmic scale in the top right box. Figure from Wilms (1998).

3.1.3. Scientific data from PCA

In this part we want to describe which PCA-data files are used in our observations and what their properties are.

We utilize a certain data format of our PCA observations. This data format is the STANDARD2F format used for scientific tasks that do not need a timing resolution better than 16 s. In this format data are binned regularly all 16 s to a 129–channel spectrum. The data is stored in the so called *science array*, that is not as voluminous as the other storing possibilities, where exact timing properties would be saved. Although the PCA allows a timing resolution of about 1 μs, we do not need that accuracy to determine the general behavior of the X-ray source GX 339−4. Instead we are interested in the good spectral resolution that this mode offers.

We only use data from PCU 2, because that is the only Proportional Counter Unit that has not experienced major problems during the lifetime of RXTE (Jahoda et al., 2006). PCU 2 is also the best calibrated PCU. PCU 0 lost pressure since the beginning of the year 2000 probably due to a micrometeorite impact. PCU 3 and 4 had periodic discharge events since 1996 and PCU 1 since 1999. To prevent this the spacecraft roll angle has been changed slightly to increase the solar heating and if not needed the PCUs 1,3 and 4 were shut down (Jahoda et al., 2006). So it is reasonable that we only used PCU 2 in our evaluations.

Furthermore we only used the top Xenon layer, because its signal-to-noise ratio is best in comparison to the two other layers. We loose some effective area when we proceed like that, so we should not go

this way for very faint X-ray sources. Fortunately GX 339−4 is not such a faint X-ray source and we can improve our datasets by using only the top Xenon layer.

Further details can be found in `https://heasarc.gsfc.nasa.gov/docs/heasarc/ofwg/docs/spectra/ogip_92_007/node6.html`.

3.2. High Energy X-ray Timing Experiment (HEXTE)

The High Energy X-ray Timing Experiment (Rothschild et al., 1998), built by the Center for Astrophysics and Space Sciences (CASS) at the University of California at San Diego (UCSD), consists of two clusters A and B of four detectors each, shown in Fig. 3.1. An enlargement of one of those NaI(Tl)/CsI(Na) phoswich scintillation detectors is shown in Fig. 3.6. More information about such detectors can be found in Gerthsen et al. (1993).

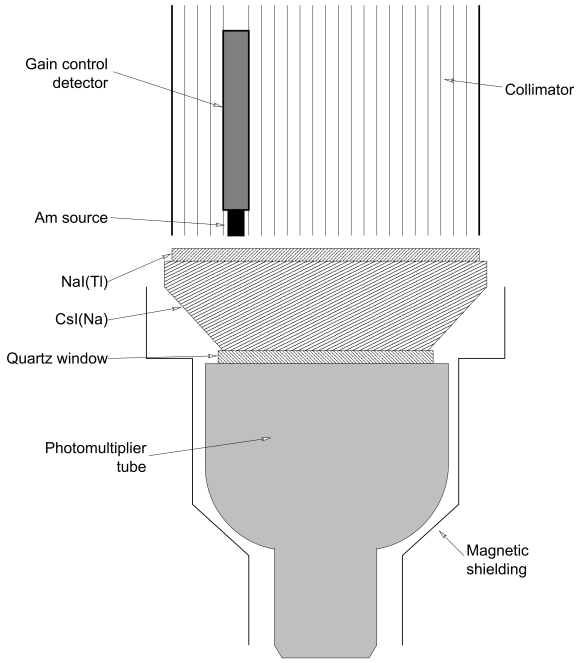

Figure 3.6.: Sketch of one of eight HEXTE detectors. On the upper side there is the collimator with a field of view of $\sim 1^\circ$. An ^{2}41Am calibration source is located within the collimator. The crystal structures with different tasks are below the collimator: The upper layer is NaI doped with Tellurium that detect the incoming photons from the X-ray source through excited scintillation light. The lower layer is CsI that detects background photons coming from the bottom or the side. The different decay times in the two crystals (NaI: 0.25 µs; CsI: 1 µs) can be used to determine whether a photon comes from a X-ray source or is background. The photomultiplier then amplifies the produced scintillation light. A magnetic shield protects the detector from further troubling influences, see Kreykenbohm (2004, page 74). Figure from Wilms (1998).

3.2.1. Background radiation

The HEXTE *external* background, e.g., diffuse X-ray background of unresolved sources or induced radioactivity from SAA[3] (see Fig. 3.7), is addressed with a swapping mechanism of HEXTE. While one HEXTE cluster directly observes the X-ray source, the other cluster observes the blank sky in the direct vicinity to obtain a background spectrum. Every 16 s or multiples of it both clusters exchange their position with the constraint that the X-ray source is observed permanently. This is achieved by a rocking mechanism: Each cluster can be displaced from its normal position by a displacement of 1.5° or 3.0°. The *internal* background is reduced by the phoswich design of the detector so that only that scintillation light is counted which is detected in the NaI crystal. Furthermore the magnetic shield reduces the background, but nevertheless the internal background is responsible for more than 95% of the total background. The total background radiation of the HEXTE detectors is much higher than the PCA background radiation. Normally the background is even stronger than the real signal (sometimes more than 100 times stronger), thus we have to understand the background really well to be able to properly use the instrument. The high dead time due to the paralyzed analog circuitry (which is needed for energy determination) after incoming high energetic photons in the NaI crystal contributes to the large background and shortens the observation time to about 60%, i.e., the effective observation time is about 40% shorter than the nominal exposure. An image of the total background of HEXTE is shown in Fig. 3.8 (left). More details about background radiation can be found in Rothschild et al. (1998).

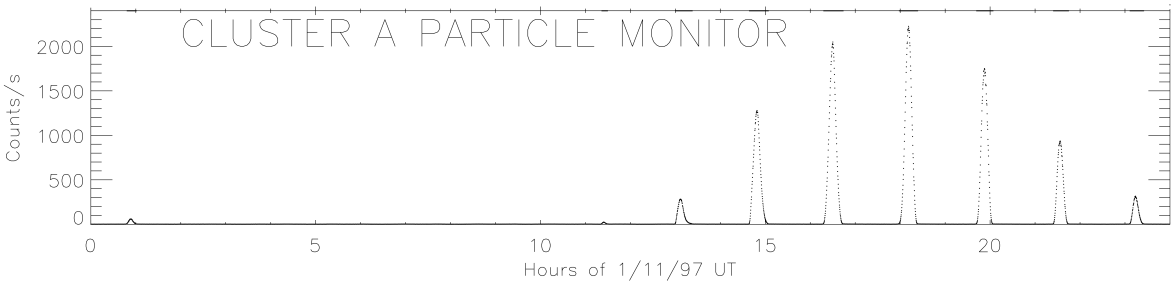

Figure 3.7.: Charged particle background rate above 0.5 MeV energy loss. Peak count rates are enlarged while transiting the South Atlantic Anomaly. Figure from Rothschild et al. (1998).

3.2.2. Energy resolution and limits

The RXTE-HEXTE has a source detection range from less than 1 mCrab = 15 keV s^{-1} cm^{-2} in a 20 keV energy band centered around 100 keV using an observation length of 10^5 s. The upper detection limit is restricted only by the total telemetry rate, that is 23,000 bits s^{-1} (Rothschild et al., 1998). Above that limit some data has to be thrown away or binned. The average energy resolution at 60 keV is about 15.4%. With an energy dependence of $E^{-1/2}$ after Wilms (1998) follows:

$$\frac{\Delta E}{E} = 0.154 \cdot \left(\frac{E}{60\,\mathrm{keV}} \right)^{-1/2} \tag{3.2}$$

HEXTE works in an energy range from 15 to 250 keV. Each of the eight detectors has an effective area of 200 cm^2 (see Fig. 3.8 right side). Because soon after the start of RXTE the pulse-height analyzer

[3]While passing the SAA the bias voltage is lowered by a factor of four to take care of the instruments

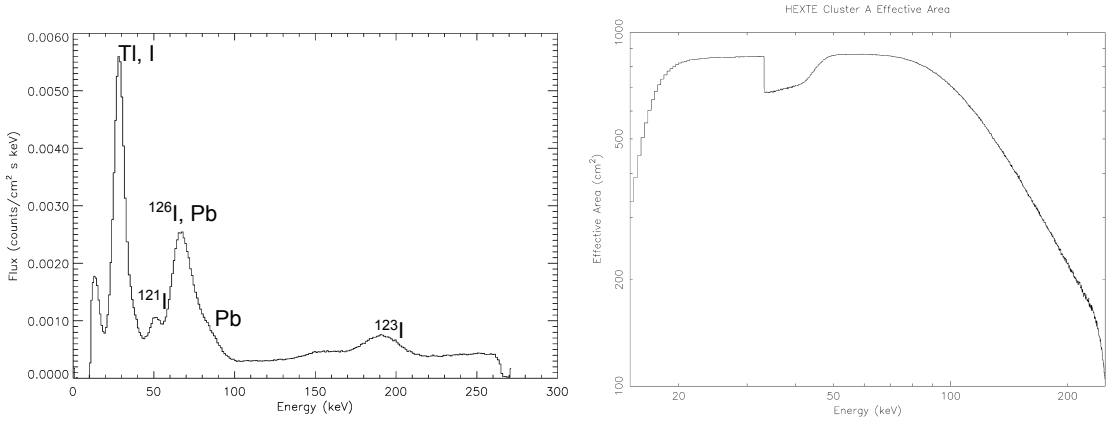

Figure 3.8.: Left: HEXTE background for one detector. The lines at 30, 55, 66 and 190 keV are caused by the activation of iodine, the lines at 74 (not visible here) and 85 keV (hard to see) indicate the K$\alpha\beta$ lines from the lead collimator. Figure adapted from Rothschild et al. (1998). **Right**: Effective area of the HEXTE A cluster. The reduction at lower energies is due to photoelectric absorption in the housing above the detector, while the reduction at higher energies is due to the finite NaI(Tl) thickness. The sharp drop and smooth recovery near 30 keV comes from the photoelectric cross section at the K edge of iodine and the onset of K-espace losses. Figure from Rothschild et al. (1998).

of one detector from cluster B failed, so the combined area is about 1,400 cm^2 at 50 keV instead of 1,600 cm^2. The temporal resolution of HEXTE is about 7 µs.

3.3. Summary

Finally we can conclude that RXTE's main capability is the feasible ultra-fast timing studies, complemented by a broadband spectral coverage with a modest spectral resolution. A last point that has to be mentioned is the normalization difference between HEXTE and PCA. HEXTE persistently evaluates spectra that are about 25% below the spectra observed by PCA. A possible explanation could be a slight misalignment of the HEXTE collimators and thus a too large estimated effective area (Wilms, 1998). As the spectral shape is not affected by that, we decided to take a multiplicative constant when simultaneously using spectra from PCA and HEXTE, shown in the spectral fits of GX 339−4 to account for the difference. Such spectra can be seen in the Figs. 4.1 and 4.2.

Chapter 4

Spectral investigation

Science is wonderfully equipped to answer the question 'How?' but it gets terribly confused when you ask the question 'Why?' *Erwin Chargaff*

In this Section we concentrate on our fit results from the various models. For this purpose we provide a part about our spectral models at first.

4.1. Spectral models

The two spectral models we used in this work are described in this segment. We used purely empirical models as we said in Sect. 2.3.2. Their goodness exceeds the goodness of fits of more complex Comptonization models, especially in the hard state. Wilms et al. (2006) proved that for Cyg X−1. In the soft states the power law fits still deliver a very good description above 6 keV. Below 6 keV, when the accretion disk becomes important, the descriptions of Comptonization models fit better (Wilms et al., 2006). At first, before we want to show the differences between the two used models (a simple powerlaw and a broken powerlaw), we give a short overview of the additional components of our spectral fits. Our models look like that:

TBNEW*(DISKBB+SIMPLEPOWER/BKNPOWER+EGAUSS)

All models, except TBNEW, can be looked up in the alphabetic summary of the XSPEC models[1]. The components are described below here and in the Sects. 4.1.1 and 4.1.2:

1. TBNEW: The model tbnew is an improvement to earlier models, especially to the model tbabs. Tbabs (Wilms et al., 2000) is a model that can explain the interstellar absorption[2] and reproduces the observed extinction appropriate in the interstellar medium (ISM). For that reason abundances of elements were prepared (see Wilms et al., 2000 table B2 and references therein) as well as depletion factors, i.e., the fraction of gas to "solid" dust grains for each element. Tbnew improves the resolution of the cross sections so this model is designed for modern spectroscopy such as modelling Fe-/Ne-/O– K-edges[3].

[1] `https://heasarc.gsfc.nasa.gov/xanadu/xspec/manual/XspecModels.html`

[2] Tbabs can also be used for intrinsic absoprtion

[3] for more details see `http://pulsar.sternwarte.uni-erlangen.de/wilms/research/tbabs/` and references therein

2. DISKBB: The spectrum of an accretion disk consists of multiple blackbody components. A disk is especially necessary in the soft state. Already in the year 1986 Makishima et al. compared the soft state spectrum of GX 339−4 fitted with a disk blackbody model with other possibilities (e.g., a powerlaw model, ...) and found that the disk blackbody model fitted the data best, especially in the soft X-rays below 3 keV (Makishima et al., 1986). This is seen as an evidence for the existance of an accretion disk in the soft state. The exact mathematical explanation of the disk blackbody spectrum can be found in Kubota et al. (1998). The resulting bolometric flux is:

$$F_{\mathrm{bol}} = \frac{2\cos(\theta) \cdot r_{\mathrm{in}}^2 \sigma T_{\mathrm{in}}^4}{D^2} \tag{4.1}$$

Here, θ is the inclination angle of the binary system ($\theta = 0$ is face-on), r_{in} is the apparent inner disk radius. The apparent inner disk radius is correlated with the real inner radius R_{in}, i.e., where the accretion disk starts as seen from the black hole. This correlation is explained in Kubota et al., 1998. σ is the Stefan-Boltzmann constant, D the distance to the source and T_{in} the temperature at the inner edge of the accretion disk. The two fitting parameters are T_{in} and a so called "norm" of the blackbody model[4]:

$$\mathrm{norm} = \left(\frac{r_{\mathrm{in}}/10\ \mathrm{km}}{D/10\ \mathrm{kpc}}\right)^2 \cdot \cos(\theta) \tag{4.2}$$

If we assume that the distance and the inclination is constant over the time – which would not be very surprising – and the norm of the blackbody spectrum changes significantly between some observations we could conclude that r_{in} changes between that observations. We already pursued such investigations indirectly in Fig. 2.3 at the right side, where we had several possible inner radii r_{in} of the accretion disk depending on the chosen accretion model. An example are the different radii in the slab and the torodial model. With the considerations we made here it is possible that the accretion disk alters between those inner radii. Therefore the geometry of the states might also not be the same in different spectral states. Problems with that conclusion are that in very hard states accretion disks are not absolutely necessary at least not with our used energy range and given spectral resolution. However, if we fit an accretion disk in those hard states, this might lead to an apparent variation of the inner radius r_{in} even if it is not there in reality. Another problem occurs when other fit parameters compensate the norm of the accretion disk, i.e., when there is a degenarcy between disk parameters and other constituents of our model. Therefore we have to be really careful with an exact prediction of r_{in}.

3. EGAUSS: In Sect. 2.3.2 we already mentioned the broad iron line as well as the possibility to model it with a Gaussian function. Because of the imprecise energy resolution of RXTE we do not need to think about the exact shape of the iron line, a Gaussian (see equation 4.3) function is sufficient.

$$\mathrm{gauss} = \frac{K}{\sigma\sqrt{2\pi}} \cdot \exp\left(-\frac{(E - E_{\mathrm{l}})^2}{2\sigma^2}\right) \tag{4.3}$$

Here K is the norm of the Gaussian function, σ is the width that was restricted to a maximum of 1 keV. E_{l} is the position of the iron line in keV. It is fitted between 5.9 and 7.5 keV with a default value of 6.4 keV.

[4] after `https://heasarc.gsfc.nasa.gov/xanadu/xspec/manual/XSmodelDiskbb.html`.

4.1.1. Powerlaw and broken powerlaw – Equations

Our first main spectral model is a simple powerlaw with two fit parameters, where K is a normalization factor and Γ is the photon index:

$$\text{powerlaw} = KE^{-\Gamma} \tag{4.4}$$

A model that is slightly more complicated is the broken powerlaw model. With this fitting model it is possible to describe the break at high energies (typically between 7 and 15 keV, Nowak et al., 2011). The formula of the broken powerlaw is:

$$\text{broken powerlaw} = K \cdot \begin{cases} E^{-\Gamma_1} & \text{for } E \leqslant E_{\text{break}} \\ E_{\text{break}}^{\Gamma_2-\Gamma_1} E^{-\Gamma_2} & \text{for } E \geqslant E_{\text{break}} \end{cases} \tag{4.5}$$

with K the normalization factor, Γ_1 the photon index for energies below E_{break} and Γ_2 the photon index for energies above E_{break}. So Γ_1 is comparable with the Γ of the powerlaw model. E_{break} is the energy of the break in the spectrum.

4.1.2. Powerlaw and broken powerlaw – Discussion

The powerlaw model only has two fit parameters while the broken powerlaw model has twice as much fit parameters. Whether this is an advantage or disadvantage, can be seen in the further information about the goodness of fits in Sect. 4.2 and in the Sect. 4.3 exemplified by the accretion disk. Fig. 4.1 shows a typical spectrum observed in four different observations that we get with the simple powerlaw model. We clearly see the different slopes of the powerlaw. We observe that the brightest observation at 3 keV is the faintest at 50 keV (this observation is shown in black) and vice versa. For comparison we fitted the same spectra with the broken powerlaw model, see Fig. 4.2. At first sight we do not notice any differences, but if we look at the photon indices of the observations we see a deviance from the fits done with a simple powerlaw. The broken powerlaw photon indices, Γ_1 , are 0.3 to 0.8 bigger than the powerlaw photon indices. For the exact reasons and further information see Sect. 4.2. In our fits we used the following specifications for PCA and HEXTE in table 4.1.

	PCA	HEXTE
energy range [keV]	2.5 – 40	25 – 250
signal-to-noise ratio (SNR)	5	3
systematic errors [%]	0.3	none

Table 4.1.: Fit specifications

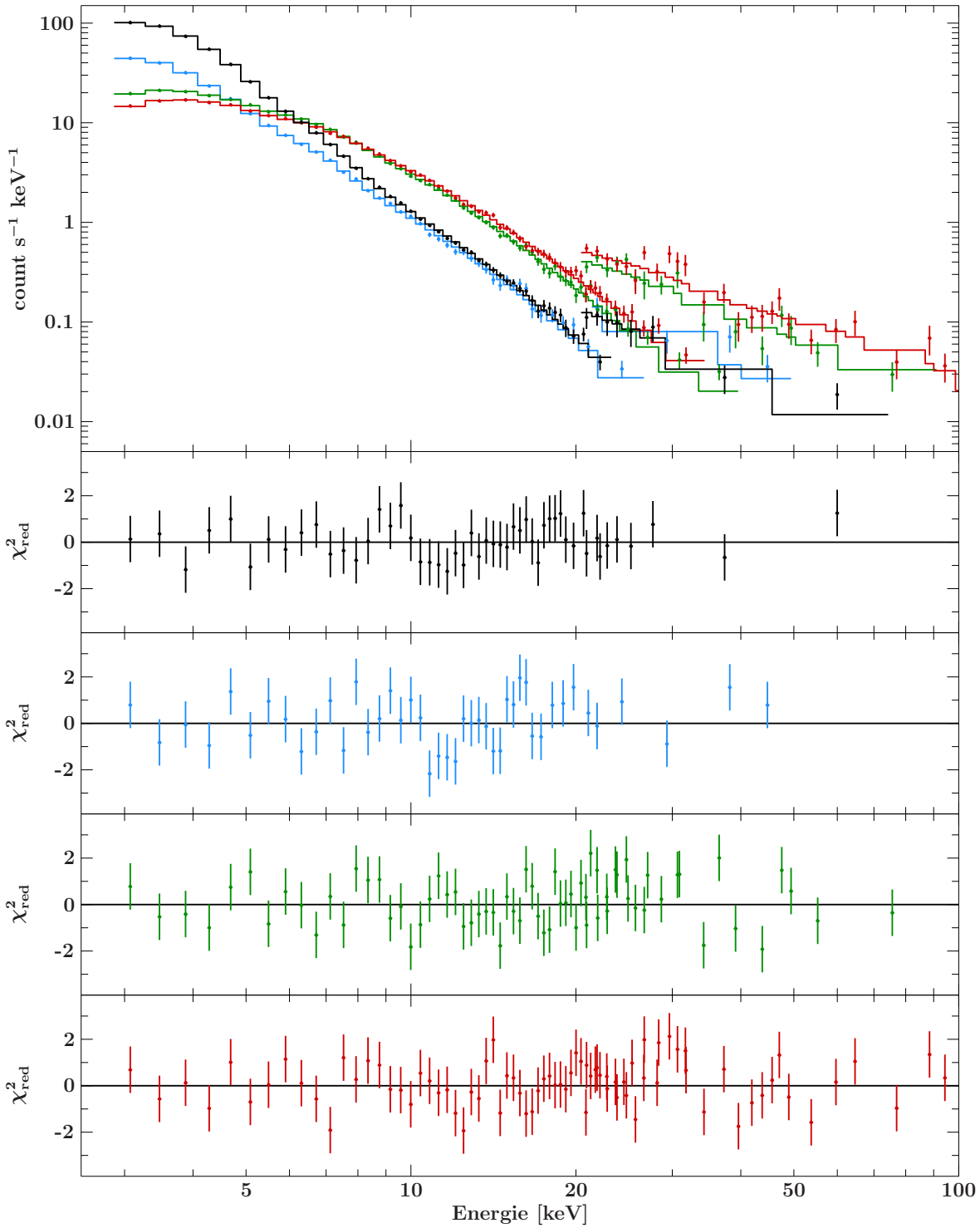

Figure 4.1.: Powerlaw spectra. The **upper panel** shows the spectra of four different obsids with four different photon indices that range from very hard to soft observations. The black line is the softest observation with $\Gamma = 2.30$, the blue and the green line have intermediate photon indices of $\Gamma = 2.14$ for the blue and $\Gamma = 1.95$ for the green line. The red line is taken out of a very hard state of GX 339−4 and has a photon index of $\Gamma = 1.68$. The four **lower panels** each show the residuals of the powerlaw model (Black: $\chi^2_{red} = 0.65$; Blue: $\chi^2_{red} = 1.38$; Green: $\chi^2_{red} = 1.21$; Red: $\chi^2_{red} = 1.00$). The black, blue and red observation have a comparable flux of 1.02 – 1.15 keV cm^{-2} s^{-1} in the energy band between 3 and 50 keV. The blue line has a slightly different flux of 0.64 keV cm^{-2} s^{-1}, because in the data sample there is no obsid that has a photon index of about 2.1 and a flux between 0.7 keV cm^{-2} s^{-1} and 1.7 keV cm^{-2} s^{-1}, so we had to choose this observation. All four fits include an accretion disk.

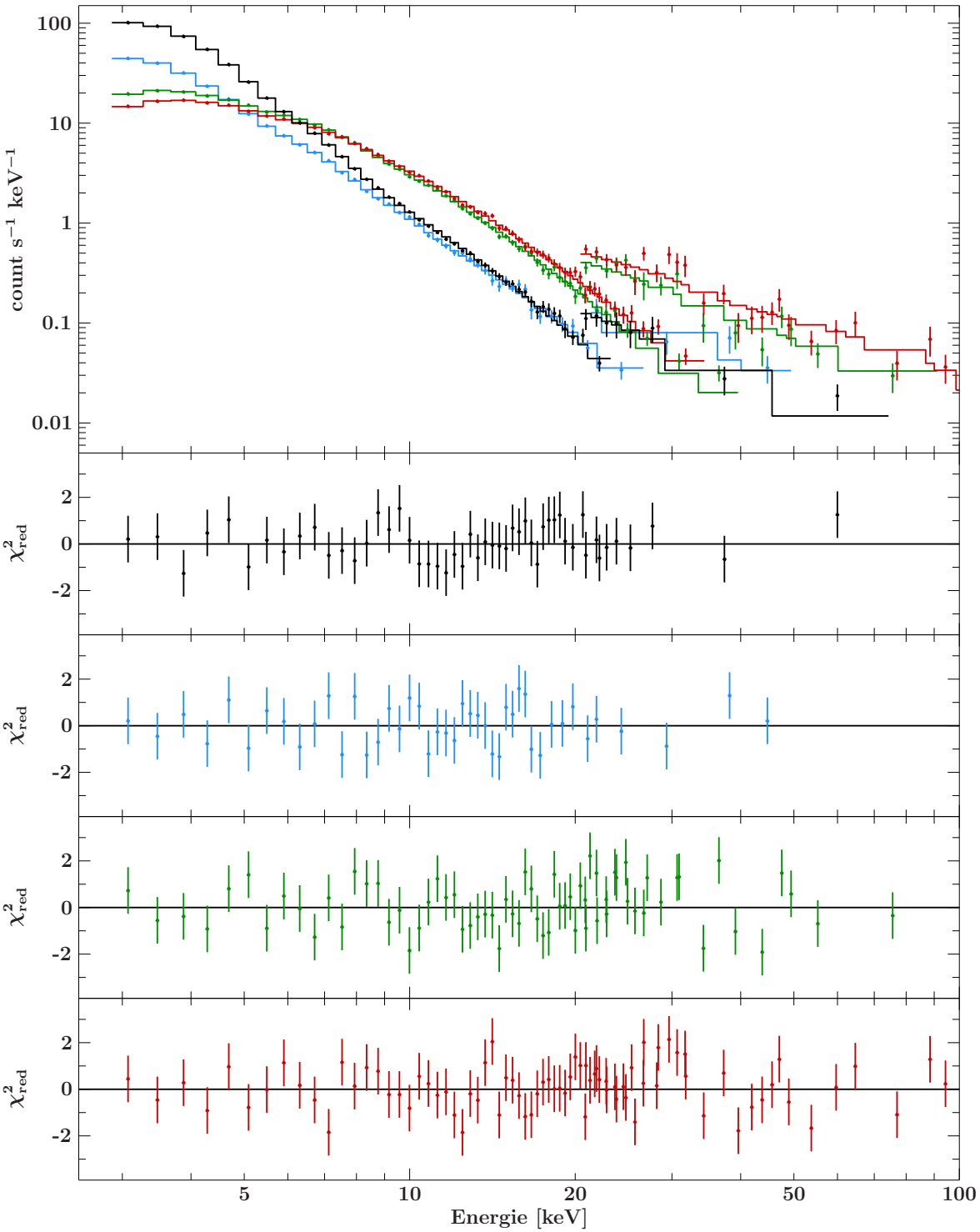

Figure 4.2.: Broken powerlaw spectra. The **upper panel** shows the spectra of four different obsids with four different photon indices that range from hard to soft observations. The same observations as in Fig. 4.1 were taken. The black line again is the softest observation with $\Gamma_1 = 3.01$, the blue and the green line have almost identical intermediate photon indices of $\Gamma_1 = 2.76$ for the blue and $\Gamma_1 = 2.72$ for the green line. The red line is taken out of a hard state of GX 339−4 and has a photon index of $\Gamma_1 = 1.96$. The four **lower panels** each show the residuals of the broken powerlaw model (Black: $\chi^2_{red} = 0.44$; Blue: $\chi^2_{red} = 0.98$; Green: $\chi^2_{red} = 1.11$; Red: $\chi^2_{red} = 0.99$). The black, blue and red observation have a comparable flux of 1.07 – 1.22 keV cm^{-2} s^{-1} in the energy band between 3 and 50 keV. The blue line has a slightly different flux of 0.69 keV cm^{-2} s^{-1}. All four fits include an accretion disk.

4.2. Powerlaw and broken powerlaw – Two "fitting" models?

4.2.1. Goodness of fits

In this Section we want to concentrate on our used spectral models, the simple powerlaw and the broken powerlaw which we introduced in Sect. 4.1.1. We wonder, if both models meet our expectations. Furthermore we want to give some tips and tricks on how to gain good fits. So, at first, let us look at the data sample of this thesis. The investigated data sample contains one major outburst in brightness and one minor post-flickering, see Fig. 4.3 or see here[5].

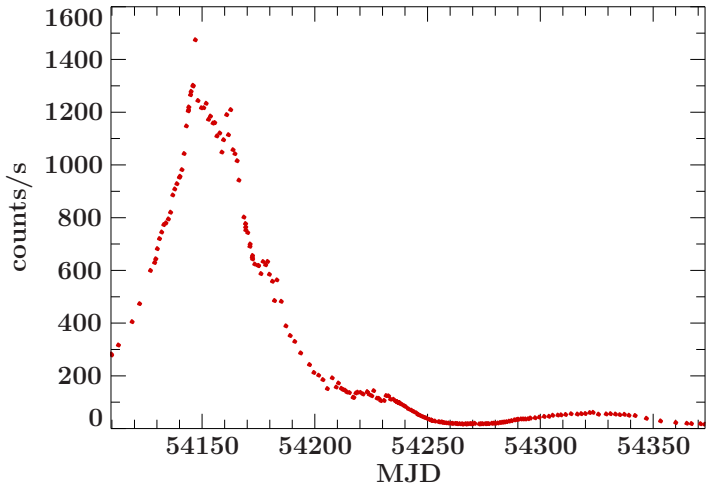

Figure 4.3.: Data sample of this thesis with one major outburst (from the beginning of our oservations at 54120 MJD to about 54250 MJD) and one minor flicker (from 54290 MJD to 54350 MJD) after the major outburst. The y-axis describes the countrate from PCA in counts per second in a given pointed observation (obsid). Every point in the plot marks one obsid. On the x-axis the modified julian date (MJD) is plotted. The MJD is a steady ongoing clock that does not account for, e.g., intercalary days. Translated in years the observations took place from the 22th of January 2007 until the 30th of September 2007. Note the flux difference during the outburst for example at 54150 and the quiescence at 54270 MJD. Its flux differs by a factor of nearly 100.

So, after that, let us go on with a schedule of performed fits during this thesis, see table 4.2. This table shows averaged χ^2_{red} only with automated fits and no correction of the fits by hand. The Figs. 4.4 show the distributions of χ^2_{red} below 3. We go this way to disentangle which of the used spectral models has the lowest error-prone and can therefore be used with less hand work.
Let us now come to the results of the fits. First we must say that the fits done with the broken powerlaw model yield better results than the powerlaw model. This is immediately understandable, if we remember that the broken powerlaw has four free fit parameters (see equation 4.5) while the simple powerlaw has only two of it (see equation 4.4). However, too many fit parameters can also lead to some problems, because of possible correlations and degeneracies between fit parameters. So the fit model can suffer of over-determination. Hence, a good strategy for pushing fits to the statistical limits is to take a model that is as simple as possible. For example let's say we choose a powerlaw model with interstellar absorption. Of course we will see that this model hits its limits very quickly. A problem would be the missing iron line at 6.4 keV (see Sect. 2.3.2, iron line). So we add the iron line to our model and re-fit everything. This game can equally be played with other parts, e.g., with an accretion disk or a break in the powerlaw, etc.. While adding more components, we have to look at every step, if the new component leads to a real improvement compared to the previous model.

[5] `http://www.sternwarte.uni-erlangen.de/~wilms/rxte/` under GX 339−4

model	$\overline{\chi^2}_{\mathrm{red}}$
normal fit	
powerlaw	1.85
powerlaw (pca only)	1.11
broken powerlaw	1.68
broken powerlaw (pca only)	1.09
with fit order	
powerlaw	1.58
powerlaw (pca only)	1.18
broken powerlaw	1.41
broken powerlaw (pca only)	1.01
free nH	
powerlaw	1.57
powerlaw (pca only)	1.19
broken powerlaw	1.40
broken powerlaw (pca only)	1.00

Table 4.2.: The fitmodel is found in the first column. It is marked, if both PCA and HEXTE data were fitted or PCA only. The second column shows the reduced χ^2. We show results for three fitting procedures: The first one with normal fits of the models with all fit parameters being fit simultaneously. The second with a provided fit order, i.e., a first fit without the iron line, a second fit of the iron line only and a third fit following up with all parameters free. In the third part after a fit with order, the hydrogen in the line of sight was fitted. A disk was included in all fits mentioned in this table. The number of fits with PCA and HEXTE was 168, the number of observations where a PCA data analysis was done is 216.

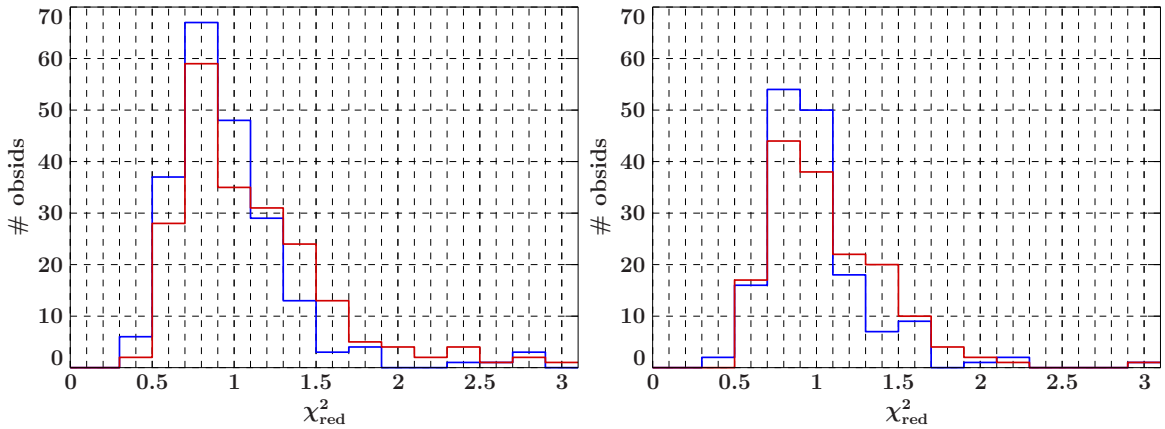

Figure 4.4.: Number of pointed observations (obsids) per χ^2_{red} for PCA (**left**) and HEXTE (**right**) data as well as for the simple (**red**) and the broken powerlaw (**blue**) model. The values for χ^2_{red} were comprised so that all values from 0.30 to 0.50 were binned to 0.40, all values from 0.50 to 0.70 were binned to 0.60, and so on. The used fits in this figures all include a blackbody disk and were performed with a "fit order" as described in the text and shown in the middle of table 4.2. Altogether we had 216 PCA and 168 HEXTE data sets, so the number of obsids in the right HEXTE panel is remarkably lower. All fits which gave a $\chi^2_{\mathrm{red}} > 3.1$ are not shown here to maintain clear visibility. In the case of "PCA/simple powerlaw" model as well as for the "PCA/broken powerlaw" model there were 4 fits that could not be fit automatically to lower values of $\chi^2_{\mathrm{red}} \leqslant 3.1$. In the case of "HEXTE/simple powerlaw model" there were 10 fits, partially with χ^2_{red} values near to 20, that could not be fitted to $\chi^2_{\mathrm{red}} \leqslant 3.1$. The "HEXTE/broken powerlaw" model showed the same trend with a slightly less number of bad fits, namely 8.

Such physical improvements can sometimes occur only in one of the states. For example, if we add an accretion disk, it yields better values solely in the soft state. To label a new fit component as "physical" we can take one of two possible paths. The first possibility is to approve a new component as physical if it leads to a $\overline{\chi^2}_{\rm red}$ closer to 1. Such a procedure was done for example by Dunn et al., 2008 (see also Fig. 4.6). Another way is to approve a component as physical if the improvement of all fits (or all fits of a certain state) is more than 2%, 3%, 5%, etc.. Otherwise the model without the component is favored.
Another point that can be read off table 4.2 is the improvement of fits if we adopt a certain order in our fits. This "order" in our case means that we first fit the continuum of the spectra without the iron line, then fit the iron line only and finally, with the obtained values by then, we fit all parameters again. This procedure yields to better $\chi^2_{\rm red}$ in powerlaw fits as well as in broken powerlaw fits, indifferent if HEXTE data is used or not. Thus, before we have to apply a new component to our models, we can perform an order-fit. In all our investigations, we therefore used these order-fits.
If we let the number of H-atoms in the line of sight, afterwards called nH, be free after such an order-fit, we do not gain a significantly better $\overline{\chi^2}_{\rm red}$ but we can try to constrain the real nH value. Unfortunately the quality of the RXTE data are not good enough to constrain the real nH value that did not converge in our fits. So we cannot say what amount of hydrogen is in the line of sight.
Another issue to be mentioned are individual bad fits that cannot automatically be fitted right and consequently have to be fitted by hand. With the simple powerlaw model these bad fits are appearing nearly as often as they appear with the broken powerlaw model. In our dataset bad fits[6] occur to about 5% of all fits, i.e., this is not a negligible number. So, after an optimized automated fit, some handwork must be done. If we do so, we get good fits in almost any observation with broken powerlaw models as well as with the simple powerlaw model. Some obsids struggle to get fit well by these models. In such cases a high energy cut off might be a good strategy to fit these obsids nevertheless. Grinberg (2013) or Wilms et al. (2006) did that for a broken powerlaw model for Cyg X$-$1 or Dunn et al. (2008) for a mixture of powerlaw and broken powerlaw models for GX 339$-$4.

We already noticed that the broken powerlaw model gives slightly lower $\overline{\chi^2}_{\rm red}$ than the powerlaw model, but nevertheless there can be greater problems with the broken powerlaw model than with the simple powerlaw. We want to discuss an example for this claim. In Fig. 4.7 we plotted the blackbody norm versus the photon index. If we do the same also for the broken powerlaw, we obtain Fig. 4.5. Comparing this with Fig. 4.7 we can state two things:

1. The basic structure, as obtained by the powerlaw model can be seen, nevertheless. But there are many more outliers than in the powerlaw model. Some of these outliers were fitted against the lower limit of the photon index[7]. This circumstance and the broader dispersion in the soft state blurres out the clarity of structures that can be seen in Fig. 4.7. They will be discussed in the according Section.

2. A second point to mention are the higher photon indices. A maximum shift of one, i.e., we get a value of 3.7 in the broken powerlaw model while we got a value of 2.7 with the simple powerlaw.

A reason for problem one can be that the broken powerlaw has four fit parameters (see Sect. 4.1.1). These are twice as many fit parameters as the powerlaw model has (see Sect. 4.1.1). So in the broken powerlaw model it is more likely that one fit parameter can be compensated by another. Exactly this circumstance can partially lead to the point cloud above $\Gamma_1 > 2.5$ in Fig. 4.5. These parameter

[6] Here we define a bad fit with $\chi^2_{\rm red} > 3$
[7] this lower limit was set to 1

degeneracies can, in part, be a reason for higher photon indices in the broken powerlaw model. As the PCA is only sensitive to energies above 2 keV, it can happen that the broken powerlaw model fits a very steep powerlaw instead of an accretion disk. So, higher Γ_1 can be achieved (Dunn et al., 2008). This issue especially occurs when the broken powerlaw model is used, because in this model the slope can first be steep and can then be flattened out towards higher energies with the aid of the break and the second part of the powerlaw model (see the two different parts of the broken powerlaw in equation 4.5). This is not an option for the simple powerlaw model and therefore an accretion disk is preferentially fitted instead of a bigger slope. On the other hand we know that the X-ray spectrum can actually have a break due to Comptonization and reflection. The broken powerlaw model can describe this physical real break, but the simple powerlaw model cannot. In such cases the simple powerlaw model might be a model that is too easy.

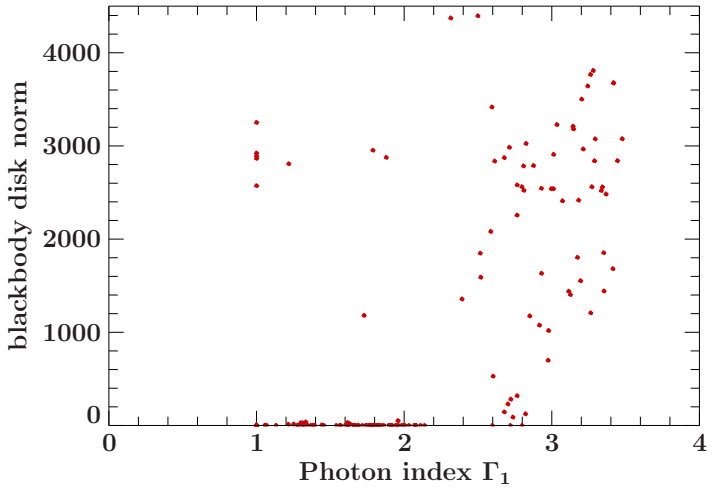

Figure 4.5.: Blackbody disk norm plotted versus photon index Γ_1 for a broken powerlaw model. The figure was equally created as the Figs. 4.7 were. Fits that were plotted against the upper limit of the blackbody norm were thrown away.

4.2.2. Best fit model

Let us remember the question asked at the beginning of this Section. Are the simple powerlaw **and** the broken powerlaw two fitting models? For answering this question we have a look at Fig. 4.6. In this figure Dunn et al. (2008) used three models, a powerlaw, a broken powerlaw and a powerlaw + disk model. Then they choose the model that works best at a certain obsid. If we want to do the same as Dunn et al. (2008), we have to be really careful otherwise we might merge our models at points where they cannot be merged at all. One example, where the powerlaw and the broken powerlaw model should not be merged, are any parts, where the photon index plays a role. But if we talk about fluxes it is fine to use both models where they work best, because the flux values are fitted to nearly equal values in the powerlaw and the broken powerlaw model, see the bottom center panel in the Figs. 4.9 and 4.11. If we weigh up on a case-by-case basis, we can decide when it is useful to merge our fit models and we can therewith conclude: Yes, the simple powerlaw and broken powerlaw model are both equally valid models that can be used at different regions to approach the statistical limit.

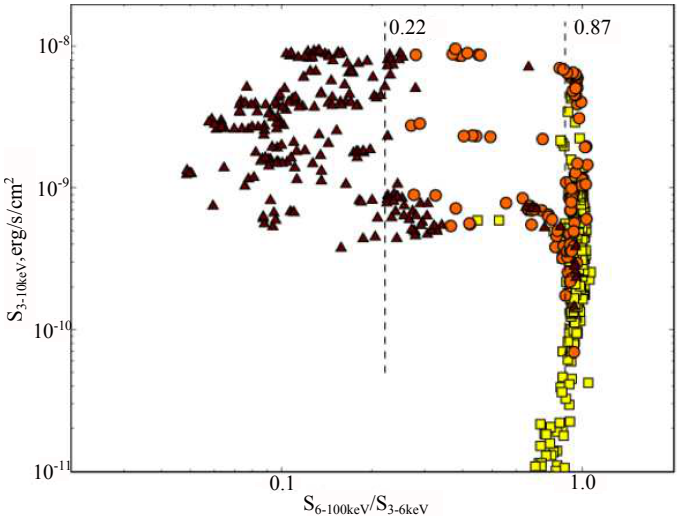

Figure 4.6.: Hardness intensity diagram for three different models where each model works best. The data points, i.e., the obsids, are taken out of a sample over one outburst. The yellow squares are from a normal powerlaw model, the orange circles from a broken powerlaw and the dark-brown triangles are from a powerlaw + disk model. The vertical lines described with 0.22 and 0.87 seperate the soft from the intermediate state and the intermediate state from the hard state. Figure adapted from Dunn et al., 2008.

4.3. Blackbody disk and state distinctions

In Sect. 4.1 we introduced our spectral models, e.g., the multicolor blackbody model for the accretion disk. Now we can pursue a first state distinction of our black hole binary. Therefore, we look at Fig. 4.7, where we plotted the photon index against the blackbody norm. As we have already seen in Sect. 2.3, the photon index can be used to distinguish the spectral states of a X-ray binary. These states can be observed in Fig. 4.7. For small photon indices we found a blackbody norm near zero as expected for hard states. That means an accretion disk is not visible in the hard state. If the photon index is larger (between 2 and 3) there are many observations that have a measurable blackbody norm. So the accretion disk can be proved in such soft states. Summarized that means with “photon indices – blackbody norm” plots we can discern between soft and hard states.

In the parts where the blackbody norm was not zero or near to zero we divided Fig. 4.7 in three different pieces as described in the following text:

1. **Sector 1**: Increase of the blackbody norm from lower to greater photon indices, in particular visible in the model with PCA data only. This perhaps shows the transition between the hard and soft state as it can be seen in the hardness intensity diagram 2.4 in the upper right corner.

2. **Sector 2**: Blackbody norm of medium height. Maybe the spread over some tenths of photon indices is due to the flickering in the soft state (also see Fig. 2.4 in the upper left corner).

3. **Sector 3**: Sector three shows the highest blackbody norms. If we go towards higher blackbody norms, a little hook tending to lower photon indices can be seen. This hook is visible in the upper left panel and if you look very closely, also in the lower left panel. The physical meaning of the little hook, if there is a physical meaning anyway, is not known.

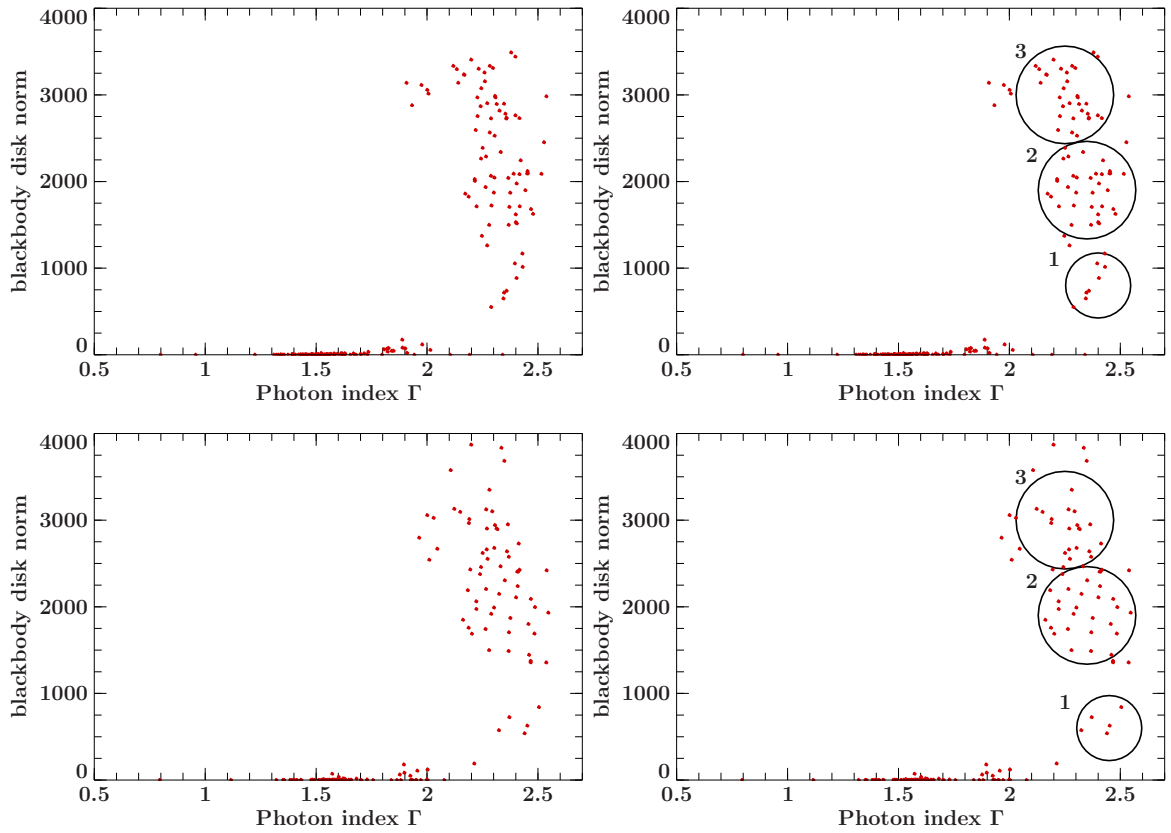

Figure 4.7.: Blackbody disk norm plotted versus photon index Γ for different models. **Upper panels**: Powerlaw model with PCA data only. On the right hand side with three marked regions. For clarity the data is shown with and without marked regions. **Lower panels**: Powerlaw model with PCA and HEXTE data. On the right hand side with three marked regions. Unphysical data, i.e., data that was fitted against the upper limit of the blackbody norm (5000), were excluded from the Figs..

4.4. Turtle-head-diagrams

4.4.1. Hardness intensity diagrams

After we investigated the spectral models in general in the previous Section, we now want to discuss more ways of distinguishing the spectral states of GX 339−4, especially considering hardness intesity diagrams (HIDs). Thereby, we already mentioned that the spectral state, also called X-ray color (Dunn et al., 2008), depends on the slope Γ of the powerlaw. If Γ is smaller than 1.8, the spectral state is a hard state, if Γ is larger than 2.0, the spectral state is a soft state. Therefore, after Fig. 2.4, we can produce a HID by plotting the photon index versus the X-ray luminosity, as we did in Fig. 4.8. We definitely see a conjunction between a classical turtle head diagram, where an energy band is divided by another one. This conjunction on the one hand can be seen in the q shape and on the other hand in the rapid changes of the color or hardness in the soft state. There is also no rapid change in color in the luminous hard state and in the return from the soft to the hard state, as expected. Opposite to a classical turtle head diagram, a strong wobble of photon indices during the underluminous hard state can be seen here. A possible explanation could be that the fit algorithm produces this wobbling of photon indices, because there are not many photons in this quiet hard state. So maybe the measured counts/s are not sufficient to constrain the photon index properly.

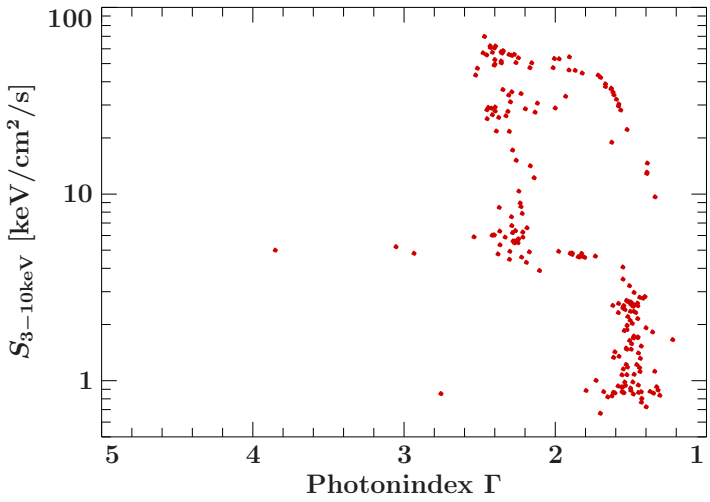

Figure 4.8.: Photon index plotted versus the X-ray luminosity with the simple power model. The outlying values in the middle have a χ^2_{red} of 0.61 – 1.26. But perhaps these observations are nevertheless fit errors. The broken powerlaw model yields much greater photon indices (reason see Sect. 4.2). Therefore, a comparison with the simple powerlaw is hard to make, so the broken powerlaw is not plotted here.

The canonical way to generate a HID is to divide a higher energy band by a lower energy band. We choose the energy bands of 3 – 6 keV, 6 – 10 keV and for the X-ray luminosity 3 – 10 keV. Figure 4.9 shows the very typical, unambiguous turtle head shaped track on the HID. On the left side the simple powerlaw model is plotted, on the right side the broken powerlaw model. As we see, the two models do not show any differences, they fit together exactly, as seen in the lower panel in the middle of Fig. 4.9. The hard state, as it is defined in Fig. 2.4, does not show any oscillations, its trend is very smooth until the source leaves the hard state. Then, at the transition between hard and soft state oscillations start rather abruptly. At this position it is assumed that the jet disappears. That can possibly explain these fluctuations, see Fender et al. (2004), Fender et al. (2009) or Belloni (2010). This argumentation is strengthened by the reverse state transition, i.e., when the source gets back from the soft to the hard state, the fluctuations immediately stop in the same way they begun. Maybe we can get further evidence of a stopping/starting jet, if we use X-ray observations parallel to radio observations[8] when a source is state transiting. In the end, it is not quite sure why the X-ray color fluctuates in the soft state. In this example we might be able to describe 'how' something happens, but in no way 'why'[9].
Altogether we perceive the different intensity between the two state transitions, i.e., from hard to soft and back. This produces the classic hysteretic form of turtle head diagrams. Thus we can state: GX 339−4 is, in respect of hardness intensity diagrams, a very typical black hole binary. Further research teams created HIDs of GX 339−4, for example Dunn et al. (2008). Their result can be seen in Fig. 4.6.

4.4.2. Variation of HIDs (DFLDs)

For comparing stellar black hole binaries Körding et al. (2006) proposed a generalization of hardness intensity diagrams, a so called "disk fraction luminosity diagram" (DFLD). The result is that active

[8] a jet can be measured exceptionally well in the radio range
[9] see quotation of Erwin Chargaff at the beginning of this Section, page 18

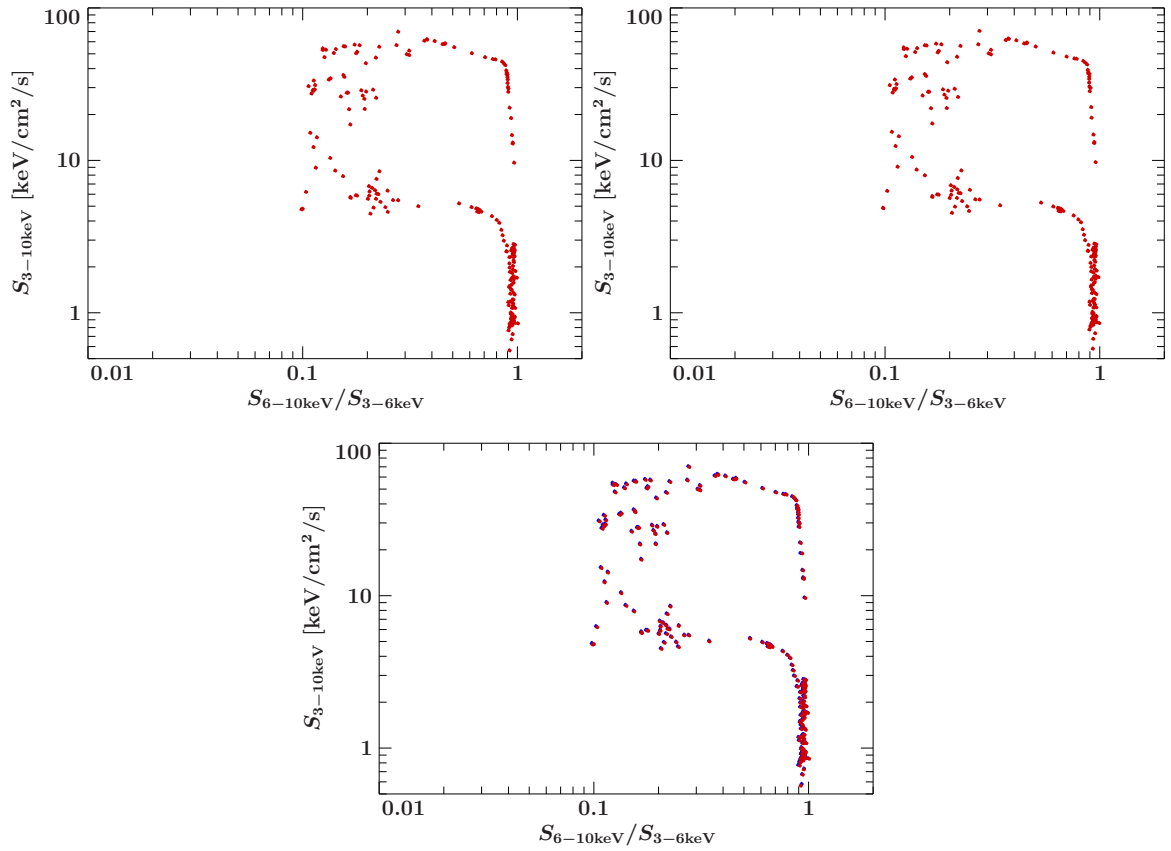

Figure 4.9.: Hardness intensity diagrams of powerlaw and broken powerlaw models. **Top left**: Simple powerlaw model; **Top right**: Broken powerlaw model; **Bottom center**: Both models superimposed, the powerlaw model on top in red and the broken powerlaw model below in blue. The two models show very little deviations. The three obsids that are located at the middle left hand side have a χ^2_{red} of 0.75 – 1.30 and are therefore probably no measurement- or fit-errors.

galactic nuclei (AGN) with their supermassive black holes can be better compared to stellar black holes. While stellar BHBs emit radiation arising from the accretion disk in the soft X-rays (0.1 to 5 keV), AGN accretion disks emit in the UV-band from 10 eV to 100 eV (Dunn et al., 2008). That means a generalization of hardness intensity diagrams is very useful, especially if we want to discern the spectral states of the source. Therefore, Körding et al. (2006) defined a "Disk fraction".

$$\text{Disk Fraction} = \frac{S_{0.1-100\text{ keV, PL}}}{S_{0.01-5\text{ keV, Disk}} + S_{0.1-100\text{ keV, PL}}} \tag{4.6}$$

where S describes the intensity in a certain energy band, here in the energy band from 0.1 to 100 keV. Furthermore we have to differentiate between the radiation from the disk and the powerlaw (PL), so these two components must be fitted individually. Dunn et al. (2008) used the unabsorbed flux as the disk flux and the absorbed flux as the powerlaw flux. The result of such a DFLD can then be seen in Fig. 4.10.

Unfortunately we cannot use the same energy ranges, as Dunn et al. (2008) have, when using RXTE, because there is no data below 2 keV. That means an accretion disk in an AGN (between 0.01 an 0.1 keV) could not be measured by RXTE anyway. But stellar black holes' accretion disks (between 0.1 to 5 keV) can be measured in part. Furthermore, compared to Dunn et al. (2008), we cannot distinguish

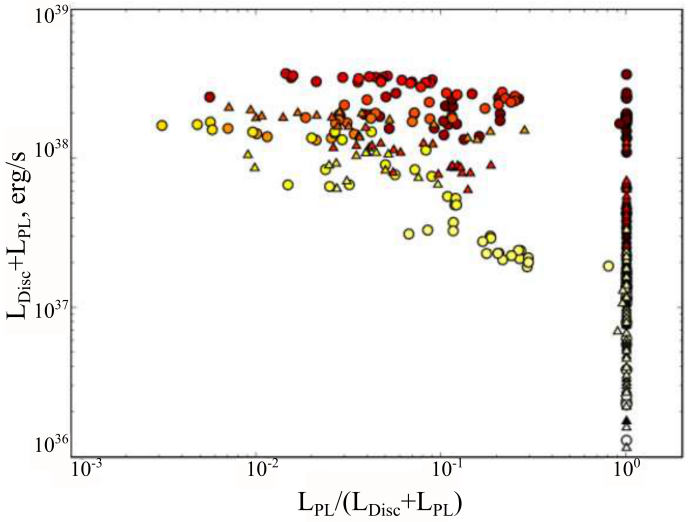

Figure 4.10.: A typical DFLD for GX 339−4 shown with a time color scheme during two outbursts. The first outburst is shown by circles, the second by triangles. Early outbursts are shown in black, late in white. So we can see the temporal behavior similar to that of a HID. The vertical line on the right hand side looking like a flag pole are observations where no accretion disk is needed to fit the spectrum properly, i.e., a typical hard state. The soft and intermediate states are in the middle and left hand side of the figure and need a disk. They mark the part looking like the flag. Figure adapted from Dunn et al. (2008).

between powerlaw radiation and disk radiation since we only have the unabsorbed flux at the time I made the DFLDs. As we want to evaluate the same data as we used in Fig. 4.9 and therewith receive comparable results, we only have PCA data between 2 and 20 keV. So our Disk fraction is altered to:

$$\text{Disk Fraction} = \frac{S_{2-20\,\text{keV}}}{S_{2-5\,\text{keV}} + S_{2-20\,\text{keV}}} \tag{4.7}$$

where we set the "equivalents" $S_{0.1-100\,\text{keV, PL}} \rightarrow S_{2-20\,\text{keV}}$ and $S_{0.01-5\,\text{keV, Disk}} \rightarrow S_{2-5\,\text{keV}}$. So we assume that the disk is solely measurable in an energy band from 2 to 5 keV. As you see, our disk fraction differs between states, where we have much disk radiation and states and where we have less. Our results are shown in the Figs. 4.11. These pictures do not look like typical DFLDs but more like HIDs. But nevertheless we can see a hard state. The intensity of the energy band at 2 – 5 keV in this state is less important than in the soft state, so this is an evidence that the accretion disk in the hard state is less important than in the soft state. We quantify this: In the hard state, where the disk fraction reaches values of nearly 0.8, the intensity of the 2 – 5 keV energy band is one quarter of the total intensity between 2 – 20 keV. In the soft state, where the disk fraction is roughly 0.55, the intensity of the 2 – 5 keV energy band reaches four fifth of the total intensity. So the accretion disk is indeed very luminous in the soft state compared to the hard state.

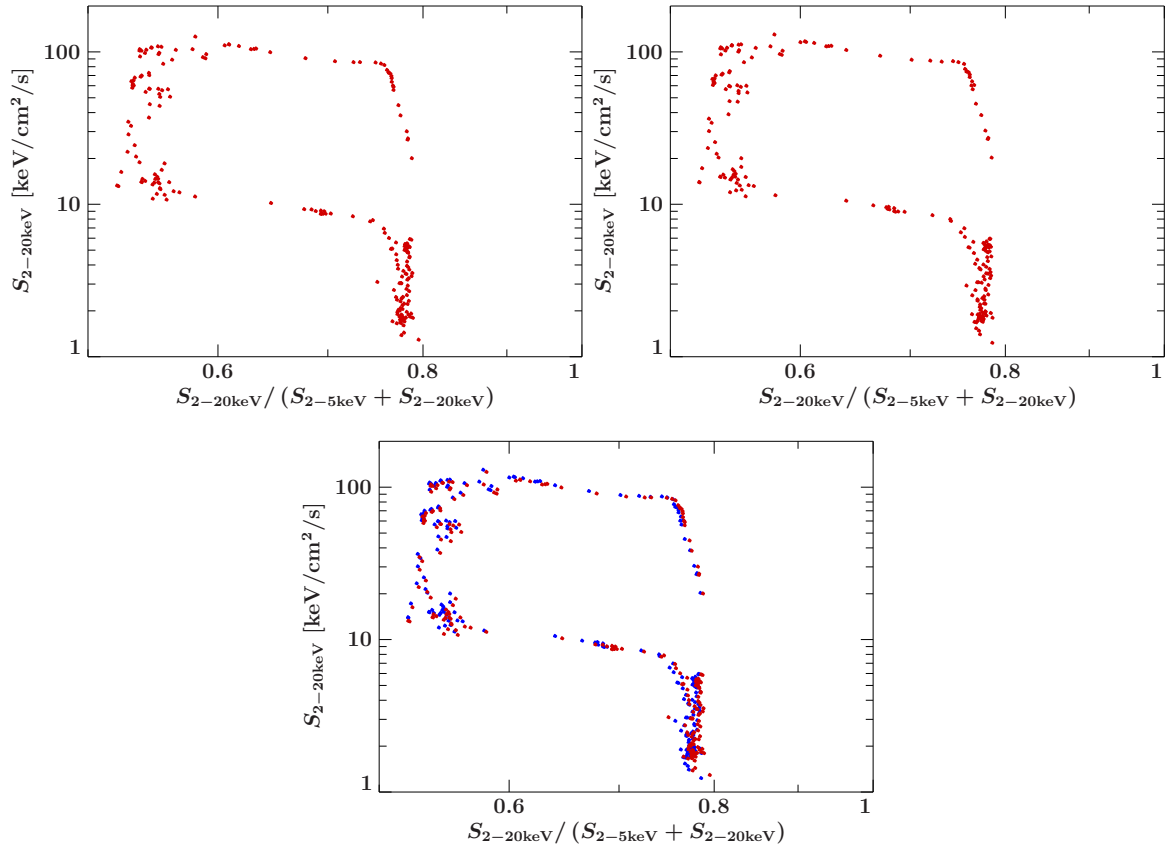

Figure 4.11.: Variation of a DFLD with powerlaw and broken powerlaw model. **Top left**: Simple powerlaw model; **Top right**: Broken powerlaw model; **Bottom center**: Both models superimposed, the powerlaw model on top in red and the broken powerlaw model below in blue. The broken powerlaw model has slightly lower disk fractions and higher total fluxes, visible in the soft state. Apart from that the two models fit together very well. The spectral states in these figures are visible as clearly as they are in normal hardness intensity diagrams.

Chapter 5

Summary and Outlook

Science never solves a problem without creating ten more. *George Bernard Shaw*

In Chapter 2 we introduced basic terms considering X-ray binaries or black hole binaries respectively. In that Chapter we also investigated the geometric appearance of BHBs. Different geometries can explain the existing phenomena equally well. There is no overall agreement on one geometry that would explain BHBs. For example the iron line is well explained by a lamp-post geometry (see Dauser, 2014) and a jet linked with it. Other possibilities prefer "sphere + disk" geometries (Dove et al., 1997) having a corona and a standard thin disk (definition of a standard thin disk see Shakura et al., 1973). So a clear distinction between different geometries is not yet possible. Looking at Fig. 2.4 it is also possible that a BHB changes its geometry between certain spectral states (see Fender et al., 2004 or Fender et al., 2009). A further point we have shown are typical physical models for spectra observed in BHB. Because we cannot distinguish between these various models, we decided to take empirical models, a simple powerlaw and a broken powerlaw model.
After that physical introduction we inserted Chapter 3 about the measuring instrument, the Rossi X-ray Timing Experiment (RXTE) and explained problems like the South Atlantic Anomaly (SAA) that have to be considered when extracting the data.
In Chapter 4 we described our used models. With each used model we plotted a spectrum, see Figs. 4.1 and 4.2. To that part we linked a discussion about the goodness of our models with the result that the broken powerlaw exceeds the simple powerlaw model. But in some issues it is helpful to use the advantages of both models as we have shown in Sect. 4.2.2. Maybe our simple and broken powerlaw models can be improved by a high energy cut off as it was performed in Grinberg (2013) or Wilms et al. (2006) for the BHB Cygnus X-1, especially if both HEXTE and PCA data are available for an observation.
Furthermore we made out disparities between the soft state and the hard state due to an accretion disk, see Figs. 4.7. Beyond that we provided some hardness intensity diagrams (see Figs. 4.9) and showed that GX 339−4 can be seen as a prototype for HIDs. With these HIDs we have the ability to discern hard from soft states as well as from hard-/soft-intermediate ones. We have shown the intensity of the disk fraction due to an accretion disk with a simplification of disk fraction luminosity diagrams (DFLDs) and found that in soft states the intensity between 2 and 5 keV is roughly three quarters of the intensity between 2 and 20 keV. With the Figs. 4.11 we can also distinguish the spectral states of GX 339−4.

Appendix A

References

Belloni T.M. (ed.), 2010, *The Jet Paradigm: From Microquasars to Quasars*, Lecture Notes in Physics, Vol. 794, Springer, Berlin

Bradt H.V., Rothschild R.E., Swank J.H., 1993, A&AS, 97, 355

Buxton M.M., Bailyn C.D., Capelo H.L., et al., 2012, AJ, 143, 16

Chen T., 2011, Proceedings IAU Symposium, 275

Corbel S., Aussel H., Broderick J.W. et al., 2013, MNRAS, 431, 107

Dauser T., Garcia J., Wilms J., et al., 2013, MNRAS, 430, 1694

Dauser T., 2014, Dissertation, in prep., *Relativistic reflection around black holes: theory and observation*, Friedrich-Alexander Universität Erlangen-Nürnberg

Dove J.B., Wilms J., Maisack M., et al., 1997, ApJ, 487, 759

Dunn R.J.H., Fender R.P., Körding E.G., et al., 2008, MNRAS, 387, 545

Fabian A. C., Rees M. J., Stella L., et al., 1989, MNRAS, 238, 729

Fender R.P., Belloni T.M., Gallo E., 2004, MNRAS, 355, 1105

Fender R.P., Homan J., Belloni T.M., 2009, MNRAS, 396, 1370

Fender R.P., Maccarone T.J., Heywood I., 2013, MNRAS, 430, 1538

Frank J., King A., Raine D.J., 2002, *Accretion Power in Astrophysics*, Cambridge, Cambridge

Fürst F., Wilms J., Rothschild R.E., et al., 2009, EPSL, 281, 125

Gallo E., 2010, *Radio emission and jets from microquasars*

Gerthsen C., Vogel H., 1993, *Physik*

Graefe C., 2014, Bachelorthesis, *X-ray analysis of Centaurus A*, Friedrich-Alexander Universität Erlangen-Nürnberg

Grinberg V., 2010, Diploma thesis, *Broadband Variability of the Black Hole Candidate Cygnus X-1*, Ludwig-Maximilians-Universität München

Grinberg V., 2013, Dissertation, *Investigations of long term variability of black hole binaries*, Friedrich-Alexander Universität Erlangen-Nürnberg

Hynes R.I., Steeghs D., Casares J., et al., 2004, ApJ, 609, 317

Jahoda K., Markwardt C.B., Radeva Y., et al., 2006, ApJS, 163, 401

Kalberla P.M.W., Burton W.B., Hartmann D., et al., 2005, A& A, 440, 775

Karttunen H., Kröger P., Oja H., et al., 2006, *Fundamental Astronomy*, Springer, Heidelberg

Körding E.G., Jester S., Fender R., 2006, MNRAS, 372, 1366

Kreykenbohm I., 2004, Dissertation, *X-ray spectra of highly magnetized neutron stars in binary systems*, Eberhard-Karls-Universität Tübingen

Kubota A., Tanaka Y., Makishima K., et al., 1998, PASJ, 50, 667

Levine A.M., Bradt H., Cui W., et al., 1996, ApJ 496, L33

Maitra D., Markoff S., Brocksopp C.,et al., 2009, MNRAS, 398, 1638

Makishima K., Maejima Y., Mitsuda K., et al., 1986, ApJ, 308, 635

Malzac J., Jourdain E., 2000, A&A, 359, 843

Miller J.M., Raymond J., Fabian A.C., et al., 2004, ApJ, 601, 450

Miller J.M., Reynolds C.S., Fabian A.C., et al., 2008, ApJ, 679, 113

Muñoz-Darias T., Casares J., Martínez-Pais I.G., 2008, MNRAS, 385, 2205

Müller A., 2007, *Lexikon der Astrophysik*, `www.wissenschaft-online.de/astrowissen/downloads/Lexikon/Lexikon_AMueller2007.pdf`

Nowak M.A., Hanke M., Trowbridge S.N., et al., 2011, ApJ, 728, 21

Oppenheimer J.R., Volkoff G.M., 1939, Phys. Rev. 55, 374

Petrucci P.O., Cabanac C., Corbel, S., et al., 2014, A&A, 564, 14

Reeves G.D., Spence H.E., Henderson M.G., et al., 2013, Science, 341 (6149), 991

Remillard R.A., McClintock J.E., 2006, ARAA, 44, 49

Rothschild R.E., Blanco P.R., Gruber D.E., et al., 1998, ApJ, 496, 538

Rybicki G.B., Lightman A.P., 1979, *Radiative processes in astrophysics*, WILEY-VCH, Weinheim

Schwarzschild K., 1916, Sitzungsberichte der Preussischen Akademie der Wissenschaften, session from 3 February 1916, 189, Berlin

Shakura N.I., Sunyaev R.A., 1973, A&A, 24, 337

Shapiro S.L., Teukolsky S.A., 1983, *Black holes, white dwarfs, and neutron stars: The physics of compact objects*, John Wiley & Sons, USA

Shaposhnikov N., Jahoda K., Markwardt C., 2012, ApJ, 757, 159

Snowden S.L., 2002, *South Atlantic Anomaly*, `http://heasarc.gsfc.nasa.gov/docs/rosat/gallery/misc_saad.html`

Tananbaum H., Gursky H., Kellogg E., et al., 1972, ApJ, 177, L5

van Allen J.A., 1958, Radiation belts around the earth (San Francisco: Freeman, 1958)

van Allen J.A., McIlwain C.E., Ludwig G.H., 1959, Geophys. Res., 64, 271

Wilms J., 1998, Dissertation, *X-rays from galactic black holes – Theory and Observation*, Eberhard-Karls-Universität Tübingen

Wilms J., Allen A., McCray R., 2000, ApJ, 542, 914

Wilms J., Nowak M.A., Pottschmidt K., et al., 2006, A&A, 447, 245

Yamada S., Makishima K., Uehera Y., et al., 2009, ApJL, 707, 109

Zdziarski A.A., Johnson W.N., Magdziarz P., 1996, MNRAS, 283, 193

Zdziarski A.A., Gierliński M., Mikołajewska J., et al., 2004, MNRAS, 351, 791

Appendix B

Acknowledgements

First of all I want to thank Prof. Dr. Jörn Wilms for the offer of this thrilling bachelor thesis and for the introduction to the circle of astrophysicists. Special thanks to you for answering my numerous questions concerning black holes and their behavior. The same thanks go to Dr. Victoria Grinberg. Although we could coordinate with each other only per E-Mail most of the time, no problems due to our spacial distance (Massachusetts Institute of Technology to Bamberg observatory) occurred. So thank you for your long and excessive E-Mails to answer my questions. I thank both of you, Mrs. Grinberg and Mr. Wilms, for your helpful advices on my bachelor thesis to improve it. Furthermore I want to thank Maria Hirsch for introducing me to ISIS and fitting X-ray spectra with this program. In this context I would like to thank Katharina Leiter for showing me how to program with ISIS and fit automatically. Thanks also to Matthias Kühnel, who answered me several questions about problems with ISIS. So thank you for your patience.

Special thanks go to Christoph Grossberger, who helped me passing my lack of knowledge in programming. I really appreciated your advices and ideas for my scripts. Additionally special thanks go to Thomas Dauser. Thanks for your great help in layouting my bachelor thesis.

Another thank you is for Manuela Meier, who assisted me in programming issues and helped improving my English. At last I want to thank my parents for supporting me during this bachelor thesis.

Thank you all – Danke euch allen !

Questions or advices? Write me an E-Mail to: `Nico.nw.Wunderling@fau.de`

This research has made use of the Interactive Spectral Interpretation System (ISIS) functions provided by ECAP/Remeis observatory and MIT. This thesis was typeset in LaTeX.